TECHNISCHE
UNIVERSITÄT
WIEN

HEPHY
INSTITUT FÜR HOCHENERGIEPHYSIK

DIPLOMARBEIT

Process Quality Control and Irradiation Studies of Silicon Sensors for the CMS Phase-II Upgrade

zur Erlangung des akademischen Grades

Diplom-Ingenieur/in

im Rahmen des Studiums

Technische Physik

eingereicht von

Veronika Kraus BSc

Matrikelnummer: 11778941

ausgeführt am

Atominstitut der Fakultät für Physik der Technischen Universität Wien und
dem Institut für Hochenergiephysik der Österreichischen Akademie der Wissenschaften (HEPHY)

Betreuung

Privatdoz. Dipl.-Ing. Dr.techn. Christoph Schwanda (TU Wien)
Univ.Lektor Dipl.-Ing. Dr.techn. Thomas Bergauer (ÖAW / HEPHY)

Wien, February 9, 2023

(Unterschrift Verfasser/in) (Unterschrift Betreuer/in)

Die approbierte gedruckte Originalversion dieser Diplomarbeit ist an der TU Wien Bibliothek verfügbar
The approved original version of this thesis is available in print at TU Wien Bibliothek.
TU WIEN Bibliothek Your knowledge hub

Acknowledgments

First of all, I would like to thank the entire HEPHY for the friendly and scientifically enriching working atmosphere. Special thanks go to Thomas Bergauer and Marko Dragicevic, who made this work possible in the first place. In numerous weekly meetings, they set the direction of this thesis and were always on hand to give me new input and advice. In addition, thanks to Thomas' initiative, I was able to receive financial support from FEMtech, which promotes women in research and technology, during the course of my work. I would also like to express my gratitude that during my time at HEPHY, I was encouraged to present parts of my work to the scientific community. These first steps of my scientific career were always strongly supported. This work also benefited from the CMS collaboration and especially the HGCAL group.
Furthermore, a big thanks to Konstantinos Damanakis for his commitment, without him the two intensive weeks for the X-ray studies at CERN would not have been possible.
Moreover, thanks to Andreas Bauer and Bernhard Arnold, who were a huge support with hardware and software, especially when things got stressful.
Finally, I'm also grateful to my entire family for always fuelling my curiosity and encouraging my thirst for knowledge from an early age, thus laying the foundation for my interest in physics.

Die approbierte gedruckte Originalversion dieser Diplomarbeit ist an der TU Wien Bibliothek verfügbar
The approved original version of this thesis is available in print at TU Wien Bibliothek.
TU WIEN Bibliothek Your knowledge hub

Abstract

High Energy Physics experiments use a wide range of technologies to detect the fundamental building blocks of our universe and test our current understanding of the Standard Model. The Large Hadron Collider (LHC) at the European Organisation for Nuclear Research (CERN) is the world's largest and most powerful particle accelerator. To extend the discovery potential of the LHC, a major upgrade to the so-called High Luminosity LHC (HL-LHC) will be implemented in the following years. For HL-LHC the received radiation levels of the detectors during their lifetime will be ten times larger than the currently expected limits. These new conditions require a full upgrade of the various detector systems along the LHC's 27 km accelerator ring. As part of this upgrade, the Compact Muon Solenoid (CMS) experiment will undergo a complete replacement of two of it's sub-detector systems, namely the silicon Tracker and the calorimeter end caps. Over 50000 new silicon sensors will be manufactured and integrated in the CMS detector during the next years, which requires reliable testing methods to ensure their quality and the stability of production parameters. Process Quality Control (PQC) establishes a fast and highly automated method to access sensor characteristics and additional process parameters from dedicated test structures for the Tracker and new High Granularity Calorimeter (HGCAL). Besides the actual purpose of PQC to monitor mass production of silicon sensors, the present work describes the additional application of PQC tests in the sensor prototyping phase of the HGCAL. Analyses of the measured PQC test structures from various prototypes up to recent Pre-series sensors are discussed in this thesis, which help to evaluate the most suitable sensor parameters for the final production.
A further important aspect in the development and testing phase of new silicon sensors is given by simulations of the devices. Therefore, a section of this work is dedicated to simulations of the PQC MOS Field Effect Transistor (MOSFET), which replicates the inter-channel region of the sensor. Altering the properties of the implant that separates the electrodes from each other, correlations can be identified that go beyond the possibilities offered by actual measurements.
Studies of irradiated test structures are another part of sensor characterisation to identify the altered properties of silicon induced by hard radiation as experienced in the CMS detector's environment. Microscopic irradiation damage in the silicon lattice leads to macroscopic changes of sensor properties. Thus, within the scope of this work, irradiation studies of selected PQC test structures with neutrons as well as X-Rays are described. The test structures exposed to neutron irradiation were measured with the PQC method to show its applicability for the altered properties of the irradiated devices. X-Ray studies were carried out at CERN with in-situ measurements that required to build a compact and portable measurement setup. The two kinds of particles allow a separate investigation of the influence of heavy neutrons on the bulk material compared to photons, which mainly cause surface damage.

Die approbierte gedruckte Originalversion dieser Diplomarbeit ist an der TU Wien Bibliothek verfügbar
The approved original version of this thesis is available in print at TU Wien Bibliothek.
TU WIEN Bibliothek Your knowledge hub

Zusammenfassung

Experimente der Hochenergiephysik nutzen ein breites Spektrum an Technologien um die grundlegenden Bausteine unseres Universums zu untersuchen und unser derzeitiges Verständnis des Standardmodells zu testen. Der Large Hadron Collider (LHC) der Europäischen Organisation für Kernforschung (CERN) ist der größte und leistungsstärkste Teilchenbeschleuniger der Welt. Um das zukünftige Potential des LHC zu erweitern wird in den kommenden Jahren ein umfangreicher Ausbau zum sogenannten High Luminosity LHC (HL-LHC) durchgeführt. Für den HL-LHC werden die Luminositäten, denen die Detektoren während ihrer Lebensdauer ausgesetzt sind, um das Zehnfache erhöht, verglichen zu derzeitigen Grenzwerten. Diese neuen Bedingungen erfordern eine vollständige Aufrüstung der verschiedenen Detektorsysteme entlang des 27 km langen Beschleunigerrings. Im Rahmen dieser Aufrüstung werden beim Compact Muon Solenoid (CMS) zwei der Subdetektorsysteme, der Silizium-Tracker und die Kalorimeter-Endkappen, komplett ausgetauscht. In den nächsten Jahren werden mehr als 50000 neue Siliziumsensoren hergestellt und in den CMS-Detektor integriert, was zuverlässige Prüfmethoden erfordert, um ihre Qualität und die Stabilität der Produktion sicherzustellen. Process Quality Control (PQC) für den Tracker und das neue High Granularity Calorimeter (HGCAL) bietet ein schnelles und hochautomatisiertes Verfahren zum Testen der Sensoreigenschaften und zusätzlichen Prozessparametern durch spezielle Teststrukturen. Neben dem eigentlichen Zweck der PQC, der Überwachung der Massenproduktion von Siliziumsensoren, beschreibt die vorliegende Arbeit die zusätzliche Anwendung von PQC-Tests in der Sensor-Prototyping-Phase des HGCAL. Es werden Analysen der gemessenen PQC Teststrukturen von verschiedenen Prototypen bis hin zur aktuellen Pre-Series diskutiert. Mit Hilfe der durchgeführten Messungen können die am besten geeigneten Parameter für die endgültige Produktion gefunden werden.
Ein weiterer wichtiger Aspekt in der Entwicklungs- und Testphase neuer Siliziumsensoren ist durch Simulationen gegeben. Daher ist ein Teil der vorliegenden Arbeit den Simulationen des PQC MOS-Feldeffekttransistors (MOSFET) gewidmet, der den Bereich zwischen zwei Sensorkanälen nachbildet. Durch Veränderung der Eigenschaften des implantierten Materials in der Simulation, welches die Elektroden voneinander trennt, können neue Korrelationen ermittelt werden.
Die Untersuchung von bestrahlten Teststrukturen ist ein weiterer Aspekt der Sensorcharakterisierung, um die durch Strahlung im CMS-Detektor veränderten Eigenschaften von Silizium zu untersuchen. Mikroskopische Schäden im Siliziumgitter führen zu makroskopischen Veränderungen der Sensoreigenschaften. Im Rahmen dieser Arbeit werden daher Bestrahlungsstudien ausgewählter PQC-Teststrukturen sowohl mit Neutronen als auch mit Röntgenstrahlen beschrieben. Die mit Neutronen bestrahlten Teststrukturen wurden mit der PQC-Methode gemessen, um zu zeigen, dass die Methode auch trotz der veränderten Eigenschaften der Teststrukturen anwendbar ist. Die Röntgenuntersuchungen wurden am CERN mit In-situ Messungen durchgeführt, welche die Entwicklung eines kompakten Messaufbaus erforderten. Die zwei verschiedenen Bestrahlungsarten ermöglichen eine getrennte Untersuchung der Einflüsse schwerer Neutronen auf das Sensormaterial im Vergleich zu Photonen, die primär Oberflächenschäden verursachen.

Die approbierte gedruckte Originalversion dieser Diplomarbeit ist an der TU Wien Bibliothek verfügbar
The approved original version of this thesis is available in print at TU Wien Bibliothek.
TU WIEN Bibliothek Your knowledge hub

Contents

1 Introduction **7**

2 High Energy Physics at CERN **9**
2.1 The Large Hadron Collider . . . 9
2.2 The CMS Experiment and its Phase-2 Upgrade . . . 9
2.2.1 Tracker . . . 11
2.2.2 High Granularity Calorimeter . . . 12

3 Silicon Sensors in High Energy Physics **14**
3.1 Semiconductor Physics . . . 14
3.1.1 Doping . . . 14
3.1.2 The pn-Junction . . . 15
3.1.3 Signal Generation . . . 15
3.2 Radiation damage . . . 15
3.2.1 Bulk Effects . . . 16
3.2.2 Surface Effects . . . 17
3.3 Sensors for Tracker and HGCAL . . . 18
3.3.1 Sensor Designs and Manufacturing Process . . . 18
3.3.2 Quality Assurance . . . 20

4 Process Quality Control **22**
4.1 Setup and Measurement Procedure at HEPHY Vienna . . . 22
4.2 Overview: Test Structure Set . . . 22
4.3 PQC from Sensor Prototypes to Pre-Series . . . 24
4.4 Metal-Oxide-Semiconductor Capacitor (MOS-C) . . . 25
4.4.1 Measurement Results . . . 26
4.5 Gate-Controlled Diode (GCD) . . . 28
4.5.1 Measurement Results . . . 29
4.6 Metal-Oxide-Semiconductor Field-Effect Transistor (MOSFET) . . . 30
4.6.1 Measurement Results . . . 32
4.7 Device Simulation . . . 32
4.7.1 MOSFET Device Structure and Results . . . 33
4.8 Van-der-Pauw Structures . . . 35
4.8.1 Measurement Results . . . 35

5 Irradiation Tests **38**
5.1 Tests of Neutron Irradiated PQC MOSFETs . . . 38
5.1.1 Irradiation Facility, Measurement Setup and Samples . . . 38
5.1.2 Measurement Results . . . 39
5.2 X-Ray Irradiation Campaign at CERN . . . 39
5.2.1 The ObeliX X-ray Facility and Measurement Setup . . . 40
5.2.2 Samples . . . 42

Die approbierte gedruckte Originalversion dieser Diplomarbeit ist an der TU Wien Bibliothek verfügbar
The approved original version of this thesis is available in print at TU Wien Bibliothek.
TU WIEN Bibliothek Your knowledge hub

5.2.3 MOSFET Measurement Results 42
5.2.4 Interpretation 44
5.2.5 Device Simulation 46
5.2.6 GCD Measurement Results 47
5.3 Comparison of Neutron and X-ray Irradiation Results in Terms of Bulk and Surface Damage 48

6 Conclusion and Outlook **49**
6.1 PQC Measurements 49
6.2 Irradiation Studies 49

Appendix **51**

Die approbierte gedruckte Originalversion dieser Diplomarbeit ist an der TU Wien Bibliothek verfügbar
The approved original version of this thesis is available in print at TU Wien Bibliothek.
TU WIEN Bibliothek Your knowledge hub

1 Introduction

The Standard Model of particle physics is truly successful in summarising our essential knowledge of the smallest building blocks of our universe to date. It describes all known elementary particles and the four fundamental interactions between them. Fermions and non-elementary particles built from them are, by convention, referred to as matter. Bosons mediate the interactions between particles, but can also occur independently. Many predictions of the Standard Model have been confirmed by particle physics experiments. In particular, the existence of elementary particles of the model that were first just predicted by the theory could be proven. Nevertheless, there are reasons to believe that the Standard Model is only one aspect of a bigger and even more comprehensive theory. Thus, the search continues.

CERN, the European Organization for Nuclear Research, has a special role to play in this search as world's leading and highly respected centre for research in particle physics. The largest particle accelerator at present is the Large Hadron Collider (LHC) at CERN, which went into operation in 2008. The intended purpose of the LHC are the generation and precise investigation of known and yet unknown elementary particles and states of matter. To enhance its sensitivity for indications of new physics, the LHC will increase its collision rate by a factor of five in the following years. The experiments located at collision points along at the LHC, such as the CMS detector, will also be adapted to the new high-luminosity environment with all its challenges. In Chapter 2, the LHC and the CMS experiment, as well as the necessary Phase-2 upgrade of the detector components will be presented. The main focus of this work lays on the CMS Tracker and especially the new High Granularity Calorimeter (HGCAL). For the upgrade, silicon sensors are going to be used. The next Chapter 3 describes the basic function of silicon sensors in High Energy Physics and the changes of their properties when exposed to high levels of irradiation.

Since all new silicon sensors for the CMS Tracker and HGCAL must meet high quality standards, they must be tested before being used for the experiment. An important tool to easily access process parameters and monitor the stability of the sensor production is the Process Quality Control (PQC), for which the dedicated test structure set was developed at the High Energy Physics Institute (HEPHY) [1]. In the context of this work, PQC measurements were carried out on HGCAL prototype test structure sets, with a focus on the different behaviour when different oxide types are used. Furthermore, the first test structures of the subsequently produced Pre-Series were measured and compared to the prototypes in order to determine whether the important parameters fulfil all requirements. Within the scope of this thesis, measurements and evaluation of the primary PQC test structures as MOS-Capacitors, Gate Controlled Diodes and MOSFETs are described (Chapter 4). In the discussion of the results of the most important PQC parameters, the HGCAL measurement results get compared to Tracker measurements as well. Simulations of a special test structure, the MOSFET, were carried out with a program based on Technology Computer-Aided Design (TCAD). TCAD refers to the use of computer simulations of semiconductor technologies and devices. The MOSFET is mainly

Die approbierte gedruckte Originalversion dieser Diplomarbeit ist an der TU Wien Bibliothek verfügbar
The approved original version of this thesis is available in print at TU Wien Bibliothek.
TU WIEN Bibliothek Your knowledge hub

used to test the inter-channel resistivity between two electrodes. Relevant for this is the so-called p-stop implant, which separates the electrodes in the final sensor. Through simulations, the properties of the p-stop implant can be easily changed and influences observed.

In Chapter 5 the performance of MOSFETs and Gate Controlled Diodes of the PQC test structure set is investigated after they have been irradiated with neutrons and X-rays. Such studies are of great importance for silicon sensors of the CMS Phase-2 detector components since they will need to sustain large particle fluences. Radiation damage in silicon sensors can be divided into bulk and surface components, the former being caused by heavy particles such as neutrons and protons, and the latter by photons and charged particles. Therefore, test structures are regularly irradiated with neutrons in a research reactor at the Jožef Stefan Institute (JSI) in Ljubljana. For the first time, the PQC setup was used to analyse irradiated test structures. In order to better understand damage in the oxide layer of the PQC test structures, an X-ray irradiation study of MOSFETs and Gate Controlled Diodes was planned and carried out as part of this work. The setup and measurement software were tested at HEPHY, the actual irradiation was performed during two weeks at the ObeliX setup at CERN. For the PQC MOSFET in particular, it was the first time that such X-ray irradiation tests had been carried out. By comparing the results to established theories and other studies, attempts are made to explain the effects seen on the irradiated test structures.

Die approbierte gedruckte Originalversion dieser Diplomarbeit ist an der TU Wien Bibliothek verfügbar
The approved original version of this thesis is available in print at TU Wien Bibliothek.
TU WIEN Bibliothek Your knowledge hub

2 High Energy Physics at CERN

The European Organization for Nuclear Research (CERN), located close to Geneva, is one of the largest scientific research centers in the world and provides an unique range of particle accelerator facilities that enable research at the forefront of science. The laboratory, established in 1954, has become a prime example of international collaboration with its 23 member states. In the 1980s the discovery of the W- and Z-Boson at CERN [2, 3] brought confirmation of the theory of the weak force. Further contributions to our current understanding of particle physics were the proof of direct CP-violation in 1999 [4] as well as the discovery of the famous Higgs-boson with the Large Hadron Collider (LHC) in 2012 [5, 6].

2.1 The Large Hadron Collider

The Large Hadron Collider (LHC) at CERN has a diameter of 8.5 km and is therefore the largest particle accelerator to date. The LHC synchrotron storage ring makes up the last stage of a powerful accelerator complex, that collides protons with centre of mass energies of up to 13 TeV. The particle beams in the LHC travel in opposite directions, close to the speed of light, in separate beam pipes kept at ultrahigh vacuum. Superconducting electromagnets guide them around the accelerator ring. The electromagnets in the LHC are cooled down to 1.9 K. Four large-scale experiments are located at four interaction points along the LHC, namely the LHCb, ALICE, ATLAS and CMS experiment. The last two of them are high luminosity, general-purpose detectors that address a wide range of physical questions. They use various detector systems to analyse the myriad of particles produced by collisions in the LHC. The luminosity of a particle collider is a parameter describing the number of collision events per second as

$$L = \frac{fN^2}{4\pi s_x s_y}. \tag{1}$$

N is the number of particles per beam revolving f times per second, s_x and s_y are the beam dimensions. From equation 1 it can be noticed, that the luminosity L increases with an increasing number of particles per beam. The event rate per second of a particle accelerator can then be expressed with

$$R = L\sigma, \tag{2}$$

where σ is the cross section. The present LHCs luminosity is $1 \cdot 10^{34}\,\mathrm{cm^{-2}\,s^{-1}}$. The integrated luminosity specifies the luminosity accumulated over time.

2.2 The CMS Experiment and its Phase-2 Upgrade

The Compact Muon Solenoid is a general-purpose detector at one of the four collision points along the Large Hadron Collider ring at CERN. It has a broad physics programme ranging from studying the Standard Model, including the Higgs boson, to searching

Die approbierte gedruckte Originalversion dieser Diplomarbeit ist an der TU Wien Bibliothek verfügbar
The approved original version of this thesis is available in print at TU Wien Bibliothek.
TU WIEN Bibliothek Your knowledge hub

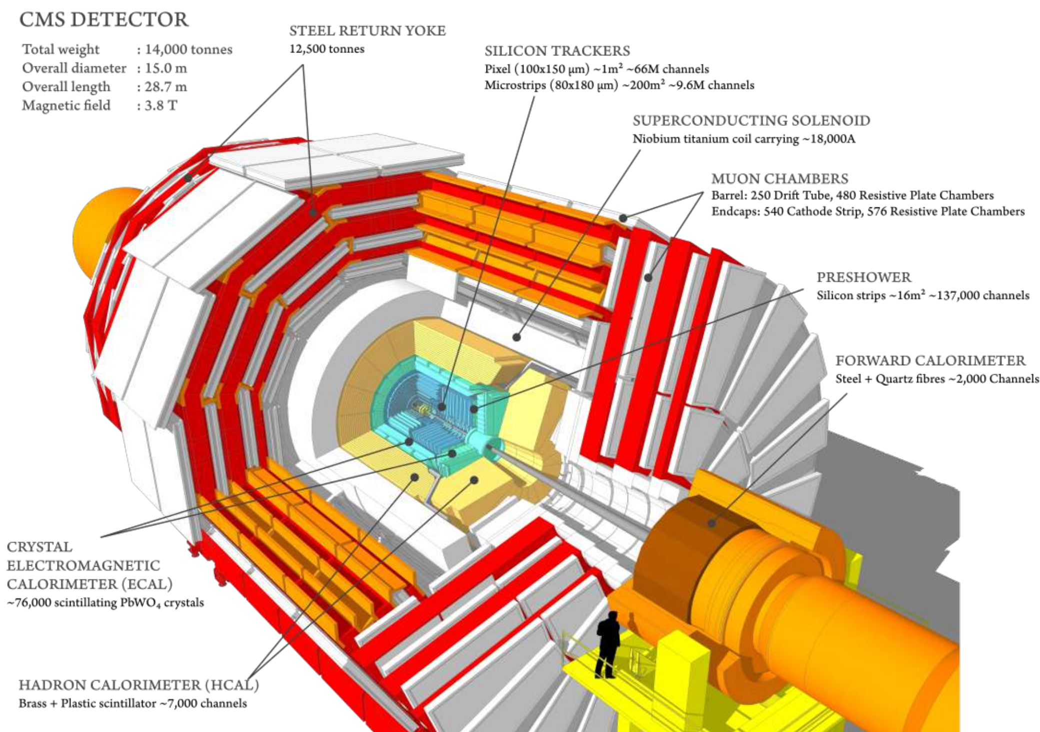

Figure 1: Schematic representation of the CMS detector composed of several concentric layers of sub-detector systems. Taken from [7].

for new physics that goes even beyond our current understanding. The CMS detector is constructed in several, cylindrical layers of sub-detector systems that allow precise measurements of all the particles produced in the proton-proton collisions of the LHC (Figure 1). One eponymous characteristic of the CMS experiment is the strong solenoid magnet which enables the determination of the ratio of momentum to mass by measuring the curvature of charged particle tracks in the magnetic field. The innermost layer of the detector is the silicon Tracker with the purpose to record the trajectories of charged particles. The next detector layers are the electromagnetic and Hadron calorimeter, which measure the energy of the primary particles and their showers. The whole energy of the initial particles is deposited in these layers resulting in the stopping of the particles in the calorimeter. The superconducting magnet surrounds the Hadron calorimeter. The outer layer of the detector is composed of muon chambers, which are the only particles that pass through the prior calorimeter layers. Therefore, the CMS detector is sensitive to all particles except neutrinos, about which conclusions can nevertheless be drawn by analysing the missing energy.

In the following years, the whole LHC is going to be upgraded to the High-Luminosity LHC (HL-LHC) to extend its discovery potential. This upgrade will increase the LHCs luminosity by a factor of five beyond the original design value ($5\cdot10^{34}\,\mathrm{cm}^{-2}\,\mathrm{s}^{-1}$). Therefore,

Die approbierte gedruckte Originalversion dieser Diplomarbeit ist an der TU Wien Bibliothek verfügbar
The approved original version of this thesis is available in print at TU Wien Bibliothek.
TU WIEN Bibliothek Your knowledge hub

Figure 2: LHC schedule including the plan for the HL-LHC upgrade. Taken from [8].

the detector systems need to be upgraded to meet the requirements of the new HL-LHC environment. The new detector systems must withstand high radiation levels, provide increased granularity and bandwidth and show an improved trigger performance. In the CMS Phase-2 upgrade, the whole tracking system will be replaced. Furthermore, the increased luminosity of the HL-LHC requires a new design of the endcap calorimeter, which is going to be replaced by the new High Granularity Calorimeter (HGCAL). The current schedule (Figure 2) for the CMS Phase-2 upgrade forsees to start with the installation of the new Tracker and HGCAL components in 2026.

2.2.1 Tracker

The new silicon tracking system can be separated into the Inner Tracker and the Outer Tracker. The Inner Tracker consists of small-size silicon pixel sensors organised into four barrel layers plus twelve discs on each end that ensure extended forward coverage. The Outer Tracker consists of silicon macro-pixel and strip sensors. It features two different types of modules: 2-S and PS. Both module types comprise two closely stacked, parallel and squared sensors. The 2-S modules are composed of two strip sensors of the same type, while the PS modules are made of one strip sensor and one macro-pixel sensor for additional resolution in the polar angle. The two new types of modules of the Outer Tracker allow transverse momentum discrimination at module level. The correlation of two hit positions at the two closely stacked sensors with a specialized readout chip enables rejection of particle tracks with low transverse momentum (Figure 3). The acceptance window for track segments of correlated signals is configured to a transverse momentum

Die approbierte gedruckte Originalversion dieser Diplomarbeit ist an der TU Wien Bibliothek verfügbar
The approved original version of this thesis is available in print at TU Wien Bibliothek.
TU WIEN Bibliothek Your knowledge hub

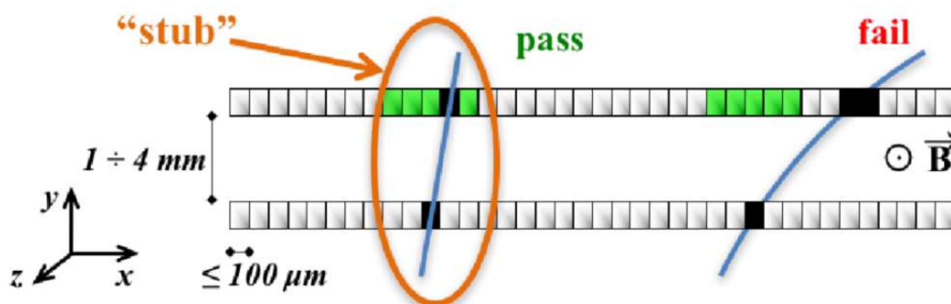

Figure 3: Correlation of signals in closely stacked Tracker sensors enables rejection of tracks with low transverse momentum. Channels in green represent the selection window. Courtesy of [9].

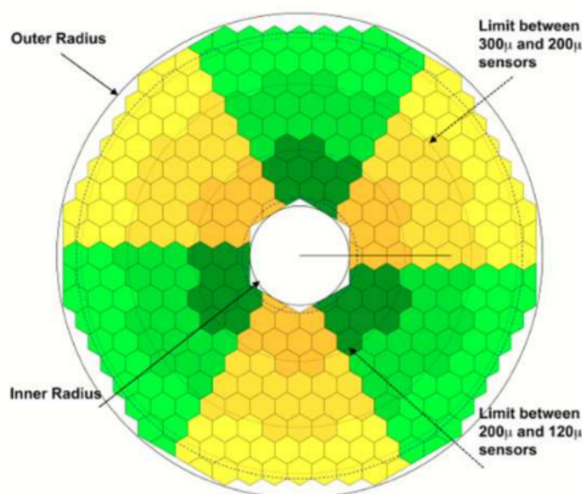

Figure 4: Single layer of the HGCAL CE-C compartment with hexagonal sensor modules. Adapted from [10].

threshold of 2 GeV. In total, the new tracking system is composed of 200 m^2 of silicon. More detailed information about the CMS tracking system can be found in [9].

2.2.2 High Granularity Calorimeter

Silicon sensors offer high granularities and are therefore also a good choice for the new HGCAL. Typical calorimeters use layers of scintillators as active material, where the spatial resolution is limited by the size of the scintillator crystals and the optical readout system. The new HGCAL will be constructed as a sampling calorimeter with both silicon sensors and scintillators as active materials. For the electromagnetic compartment (CE-E) of the HGCAL only silicon sensors are used. CE-E utilizes copper, copper-tungsten, and

Die approbierte gedruckte Originalversion dieser Diplomarbeit ist an der TU Wien Bibliothek verfügbar
The approved original version of this thesis is available in print at TU Wien Bibliothek.
TU WIEN Bibliothek Your knowledge hub

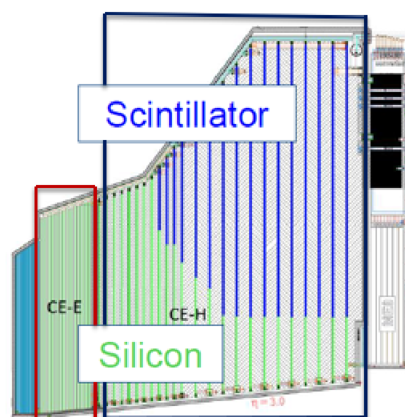

Figure 5: Cross section of the CMS HGCAL. The HGCAL is separated into an electromagnetic compartment (CE-E) and a hadronic compartment (CE-H) with areas of silicon (green) and scintillators (blue). Courtesy of [11].

lead plates clad in stainless steel as absorber material. A layer of the HGCALs CE-E compartment with its hexagonal sensor modules can be seen in Figure 4. A more detailed description of the sensor design is given in section 3.3. For the Hadronic compartment (CE-H) silicon in combination with scintillator tiles as active material is used (Figure 5). CE-H only has stainless steel as absorber material. For the final HGCAL around $600\,\mathrm{m}^2$ of silicon are needed. This work mainly focuses on testing and analysing of silicon sensors for the HGCAL, whereas Tracker sensors are mentioned for reference and for the sake of completeness.

Die approbierte gedruckte Originalversion dieser Diplomarbeit ist an der TU Wien Bibliothek verfügbar
The approved original version of this thesis is available in print at TU Wien Bibliothek.
TU WIEN Bibliothek Your knowledge hub

3 Silicon Sensors in High Energy Physics

The new CMS Tracker and HGCAL use silicon sensors for particle detection. Silicon as a semiconductor offers a lot of advantages for high energy physics like a low ionization energy, high position resolution and radiation hardness, which makes it well suited for the application in high-radiation environments such as the upgraded HL-LHC detectors. Furthermore, physics applications can benefit from the experience of the microelectronics industry, where silicon is by far the most commonly used base material for electronic devices. The following section gives an overview of the basic properties of silicon as sensor material and of the specific sensors used in the CMS Tracker and HGCAL. The explanations of the general concepts have been adapted from an introductory chapter on the topic of silicon sensors in [1].

3.1 Semiconductor Physics

Solid state materials can be distinguished by their energy band structure and can thus be divided into insulators, conductors and semiconductors. Silicon is an elemental semiconductor. It has the atomic number 14 from the 4th main group of the periodic table with four valence electrons that form covalent bonds when condensed into the typical diamond-like crystal lattice structure. At temperatures close to $T \approx 0\,\text{K}$, the electrons are bond and no free charges are available. For nonzero temperatures, thermal excitation can lift electrons from the valence band to the conduction band, leaving behind a positively charged hole. The band gap of silicon, defined as the difference of the energy level of the conduction and valence band, is $1.12\,\text{eV}$ at a temperature of $300\,\text{K}$.

3.1.1 Doping

To alter the properties of an intrinsic semiconductor, small amounts of impurities can be introduced to the silicon crystal lattice (i.e. doping). The semiconductor becomes extrinsic. In n-doping (n: free-moving negative charge), so-called donor elements of the 5th main group of the periodic table are introduced to the lattice. Four of its valence electrons contribute to the covalent bonds with the neighboring silicon atoms, one weakly bond electron of the donor is freely available and moves when applying a voltage. Introducing impurities of the 3rd main group leads to p-doping (p: free-moving positive hole), where acceptors with only three valence electrons are used. An electron fills the vacant state and creates a positive charge, referred to as a hole. When a voltage is applied, this hole behaves like a freely movable positive charge. Doping also shifts the Fermi level of the semiconductor compared to its intrinsic case. N-doping results in a shift of the Fermi level towards the conduction band, p-doping shifts it towards the valence band.

The resistivity ρ of a semiconductor is proportional to the inverse of the charge carrier concentration times their mobility

Die approbierte gedruckte Originalversion dieser Diplomarbeit ist an der TU Wien Bibliothek verfügbar
The approved original version of this thesis is available in print at TU Wien Bibliothek.
TU WIEN Bibliothek Your knowledge hub

$$\rho = \frac{1}{q(n\mu_n + p\mu_p)}. \tag{3}$$

Here, n and p represent the electron and hole concentration respectively and μ_n and μ_p their corresponding mobilities. For extrinsic semiconductors, this can be simplified to

$$\rho = \frac{1}{q\mu_n N_d} \quad \text{and} \quad \rho = \frac{1}{q\mu_p N_a}, \tag{4}$$

where N_d and N_a are the dopant concentrations.

3.1.2 The pn-Junction

One of the most fundamental semiconductor devices, also known as diode, is created by bringing p-type and n-type silicon into contact. In the contact region a charge carrier concentration gradient is produced. This leads to a diffusion of the excess electrons of the n-type silicon to the p-type region and a subsequent recombination with the holes. A space-charge or depletion region forms and an excess negative charge gets established in the p-type region while an excess positive charge gets established in the n-type region. The created potential difference suppresses further diffusion by creating a counteracting drift. In equilibrium, the two effects are balanced and lead to a finite width of the depletion region. The characteristics of a p-n junction can be modified by applying an external bias voltage. Applying a negative potential to the p-type region and a positive potential to the n-type region is called reverse biasing. This leads to an increase of the width of the depletion region in the diode.

3.1.3 Signal Generation

In general, the interaction of charged, heavy, moderately relativistic particles with matter is determined by elastic Coulomb scattering. The ionisation energy loss per unit length for a particle with velocity $v = \beta c$ is given by the well-established Bethe-Bloch formula, as can be found for example in [12].

With the loss of kinetic energy, the particle traversing the material creates electron-hole pairs (ionization energy of silicon: 3.6 eV). Position-sensitive silicon sensors are composed of lightly doped silicon base material (p-type for the CMS Phase-2 upgrade's sensors) in combination with more heavily doped implants (n^+ for the CMS Phase-2 upgrade). In operation the sensors are under full depletion, which means that the depletion region extends over the whole semiconductor width. Thus, the created charge carriers can drift in the electric field and a signal it produced.

3.2 Radiation damage

Aside from the wanted effects of ionization caused by traversing charged particles, the interactions of high energy charged and neutral particles with the detector material can

Die approbierte gedruckte Originalversion dieser Diplomarbeit ist an der TU Wien Bibliothek verfügbar
The approved original version of this thesis is available in print at TU Wien Bibliothek.
TU Bibliothek WIEN Your knowledge hub

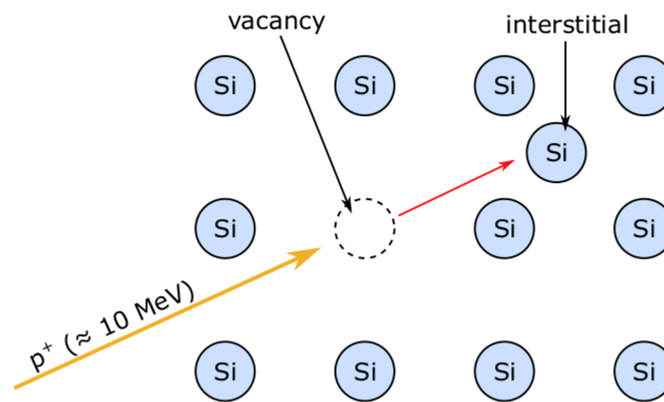

Figure 6: Displaced, interstitial Si atom and vacancy referred to as Frenkel pair. Courtesy of [1].

cause permanent damage that diminishes the detector performance over time. In the following, a brief discussion of radiation effects and the resulting, altered sensor properties shall be given.

3.2.1 Bulk Effects

Radiation effects in silicon sensors can be separated into bulk and surface effects. Bulk effects are mainly caused by non-ionizing energy loss of heavy particles like protons, neutrons and pions, which elastically collide with the atomic nuclei of the silicon lattice. If a heavy particle transfers more than 20 eV threshold energy to a silicon atom, this atom can be displaced out of the lattice site [13]. The combination of a displaced, interstitial Si atom and its vacancy is called a Frenkel pair and denotes a point defect (Figure 6). If the Si atom has enough recoil energy to displace further atoms, a defect cascade is produced. Both interstitials and vacancies are mobile at room temperature and can recombine again (beneficial annealing). Another part of the defects do not recombine and migrate through the lattice, interacting with each other or with impurities in the bulk. This process leads to stable defects at different energy levels within the silicon band gap. These defects are ultimately responsible for the altered, macroscopic properties of the silicon sensors.

The microscopic defects induced by radiation in the silicon bulk lead to macroscopic changes of the sensor properties. Different types of defects located at different energy levels of the band gap, as schematically shown in Figure 7, alter the properties in various ways. Defects located close to the conduction band act as donors whereas defects located near the valence band act as acceptors. The altered effective doping concentration of the silicon bulk results for example in changing resistivity and a changing full depletion voltage. Therefore, the doping concentration after irradiation is denoted as the effective doping concentration. Generally, both types of defects are produced, whereby during

Die approbierte gedruckte Originalversion dieser Diplomarbeit ist an der TU Wien Bibliothek verfügbar
The approved original version of this thesis is available in print at TU Wien Bibliothek.
TU WIEN Bibliothek Your knowledge hub

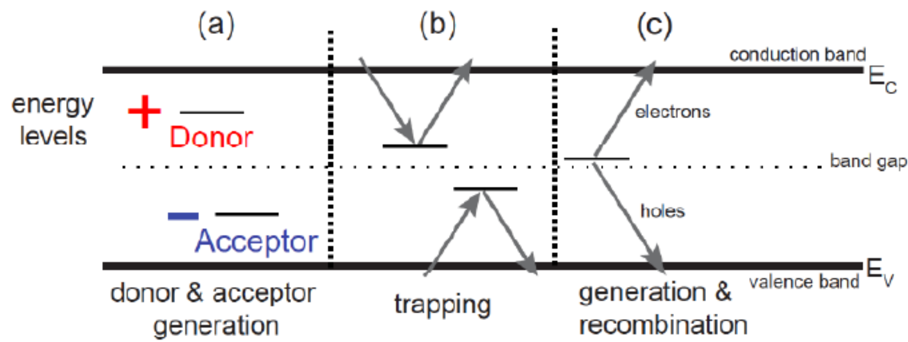

Figure 7: Schematic sketch of the band gap of silicon showing different types of irradiation defects. Courtesy of [15].

irradiation initially present donors get removed which leads to an overall increase of the acceptors [14]. In addition, generation-recombination centres in the bulk lead to an increasing leakage current of irradiated silicon sensors.

To scale and quantify the radiation damage produced by particles of various kinds and energies, the *non-ionising energy loss (NIEL) scaling hypothesis* is used [14]. The NIEL hypothesis assumes that any radiation damage in a material caused by lattice displacement scales linearly with the non-ionising energy loss of the traversing particle, which again scales linearly with the displacement energy. Thus, the radiation damage induced by different types of particles can be scaled with the NIEL hypothesis. Particularly, the fluence Φ of any particle can be scaled to the equivalent fluence of mono-energetic 1 MeV neutrons that would induce the same damage,

$$\Phi_{eq} = \kappa \cdot \Phi, \tag{5}$$

where κ is the hardness factor.

3.2.2 Surface Effects

The surface (i.e. the oxide layer and Si-SiO_2 interface) gets mainly affected by ionising radiation like photons and charged particles. Photons, with energies as expected in particle detectors, interact with silicon and silicon dioxide mainly through the photoelectric effect. In the photoelectric effect the incoming photon is completely absorbed by the target atom, which in turn releases an electron. An electron-hole pair is created. With an external electric field, a fraction of electrons and holes immediately recombine. The rest of the electrons, referred to as charge yield, have a high mobility in the silicon dioxide and collect at the electrodes. The remaining holes drift to the Si-SiO_2 interface. They get captured by oxygen vacancies and form trapped positive charges in the oxide, referred to as oxide charges. Some of the holes react with hydrogenated oxygen vacancies. When a

Die approbierte gedruckte Originalversion dieser Diplomarbeit ist an der TU Wien Bibliothek verfügbar
The approved original version of this thesis is available in print at TU Wien Bibliothek.
TU WIEN Bibliothek Your knowledge hub

positive hole interacts with a neutral hydrogen atom, positively charged hydrogen ions (i.e protons) remain. Those protons, which drift to the interface, break the hydrogenated silicon bonds at the interface and produce dangling silicon bonds, referred to as interface traps [16]. Ionisation in the oxide layer leads to an increase of fixed, positive oxide charges and interface traps which macroscopically affects the isolation between sensor channels.

3.3 Sensors for Tracker and HGCAL

The CMS Phase-2 Upgrade of the Tracker and the HGCAL will incorporate over 50 000 new silicon sensors. As already mentioned, the operation in the HL-LHC environment puts severe constraints on silicon sensor material and design, especially in terms of radiation tolerance and detector resolution. Because of its better performance under irradiation, as reported in [17], the Phase-2 Upgrade will utilize p-type silicon as base material for both, the Tracker and HGCAL sensors. The CMS collaboration has carried out R&D, prototyping and irradiation campaigns to determine the best-suited base material. Much expertise can also be drawn from experience with the silicon sensors of the current CMS Tracker. In the following, design considerations for the silicon sensors of the Tracker and HGCAL and their quality assurance shall be briefly summarized.

3.3.1 Sensor Designs and Manufacturing Process

The silicon sensors for the CMS detector get produced by Hamamatsu Photonics K.K. (Japan). Wafers are cut from high-purity, single crystal silicon ingots as base material. These wafers undergo various processing steps, including thermal treatment, photolithography, etching and sputtering. For the implants, an oxide layer is grown via thermal oxidation. Then a light-sensitive paint, the so-called photoresist, is applied on the oxide and the desired layout is projected via masks on this layer. After light exposure, the photoresist is developed. Depending on the used type, either the exposed or non-exposed parts dissolve in the developing solution. Further, the oxide layer is etched away in the regions without photoresist, leaving only the silicon. When the dopant is applied with an ion implanter, the molecules can diffuse into the wafer only in those bare regions, forming the desired patterns. These steps are repeated for all implants. The final, thick passivation layer gets applied to protect the sensor.

Both Tracker and HGCAL sensors are manufactured on p-type substrate in combination with more heavily doped n^+ implants. Moreover, all sensors use a method referred to as p-stop isolation. To ensure precise position resolution, the individual sensor electrodes have to be electrically isolated. In the sensors, positive oxide charges attract electrons from the silicon bulk that can from a conductive interconnection between individual n^+ implants. This can be prevented by introducing a p-stop implant with higher doping in between them.

The Tracker sensors are produced on 6 inch wafers and are square shaped in the final experiment. The 6 inch production process is well established since similar processes

TU Bibliothek WIEN Your knowledge hub
Die approbierte gedruckte Originalversion dieser Diplomarbeit ist an der TU Wien Bibliothek verfügbar
The approved original version of this thesis is available in print at TU Wien Bibliothek.

Sensor qualification specifications	**Tracker**	**HGCAL**
Substrate resistivity [kΩ cm]	>3.5	>3.0
Physical thickness [µm]	320	300; 200; 300
Active thickness [µm]	290	300 (FZ); 200 (FZ); 120 (epi)
Full depletion voltage [V]	<350	<370; <160; <70
Types	2S and PS-s strip sensors (AC-coupled); PS-p Macropixel sensors (DC coupled)	LH (low density), HD (high density) and Multi-geometry Wafers (all DC-coupled)

Table 1: Sensor qualification specifications and acceptance limits for the CMS Tracker and HGCAL.

have been applied for the sensors currently in use. As already mentioned, three different types of sensors exist for the Outer Tracker. For the 2-S modules, two silicon sensors of the same type are used, whereas the PS modules consist of one strip sensor and one macro-pixel sensor. The strip sensors use AC coupled readout and are biased via polysilicon resistors. For the macro-pixel sensors this is not possible due to smaller pads. Thus, they are DC coupled. Detailed sensor specifications can be found in Table 1.

The HGCAL sensors use 8 inch technology, which is a newly utilized process, since very large areas have to be covered. For the same reason, to use the maximum area of a wafer, HGCAL uses hexagonal sensor modules. At the corners of the sensor planes in the HGCAL, partial sensors are required. The corresponding wafers are referred to as Multi-geometry wafers, where the sensor can be fractioned at given lines. There are three different sensor types used at different locations inside the HGCAL, designed for different expected irradiation levels, as can be seen in Figure 8. Generally, a thicker sensor is beneficial for the readout efficiency. Nevertheless, a high voltage is required to fully deplete the whole sensor. As irradiation increases the depletion voltage, this limits the sensor's radiation hardness besides trapping, which occurs more frequently in thicker sensors. The two sensor types for regions with lower expected radiation in the HGCAL have thicknesses of 200 µm and 300 µm. Their wafers are produced with the so-called Float-Zone process. They share a common layout with 192 channels per wafer, called Low Density (LD) wafers. The third type for the inner parts of the HGCAL has an active thickness of only 120 µm. For this sensor type, the active layer is deposited on a so called substrate wafer via the epitaxial growth method. The layout for this wafer type

TU Bibliothek WIEN Your knowledge hub
Die approbierte gedruckte Originalversion dieser Diplomarbeit ist an der TU Wien Bibliothek verfügbar
The approved original version of this thesis is available in print at TU Wien Bibliothek.

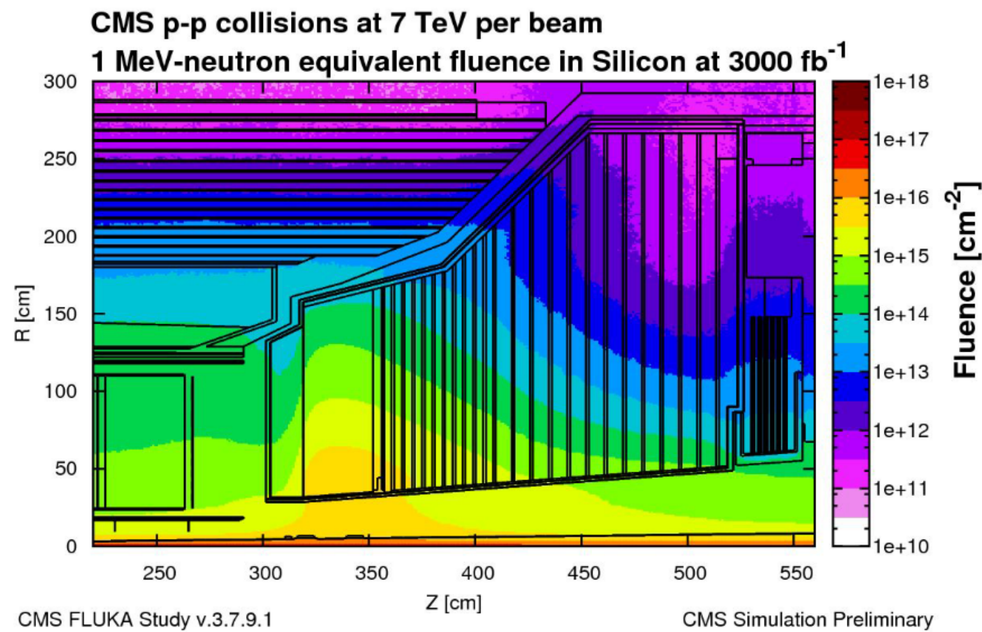

Figure 8: FLUKA simulation of the expected particle fluence in r-z view of the HGCAL. Courtesy of [18].

is different and has 432 channels for higher spatial resolution, referred to as High Density (HD). The active elements for all types of HGCAL sensors are individual hexagonal DC-coupled diodes. All cells include passivation openings at each corner to allow wire bonding to the readout board. Again, further sensor qualification specifications can be found in Table 1.

3.3.2 Quality Assurance

Since silicon sensor production is a very elaborated multi-stage process and the final sensors must meet high requirements for the final experiment, an effective quality assurance (QA) system is mandatory to control and monitor the stability of the sensor production. The quality assurance system shown in Figure 9 was first established by the CMS community for the Tracker sensors, which are, at the time of writing this thesis, already in production. For HGCAL, a similar process is planned for the soon starting production. The QA starts with Vendor Quality Control directly at Hamamatsu. Then there is Sensor Quality Control (SQC) where the test centers, including HEPHY, perform single strip and inter-strip measurements across the whole sensor. Process Quality Control (PQC) measurements on test structures from the cut-off region of each wafer will be the main focus of this work. PQC is going to be described in more detail in the following chapter 4. The advantage of process quality control is that it allows fast measurements of a dedicated test structure set and gives access to parameters that are not accessible via sensor measurements. A small fraction of the produced sensors undergo irradiation

Die approbierte gedruckte Originalversion dieser Diplomarbeit ist an der TU Wien Bibliothek verfügbar
The approved original version of this thesis is available in print at TU Wien Bibliothek.
TU WIEN Bibliothek Your knowledge hub

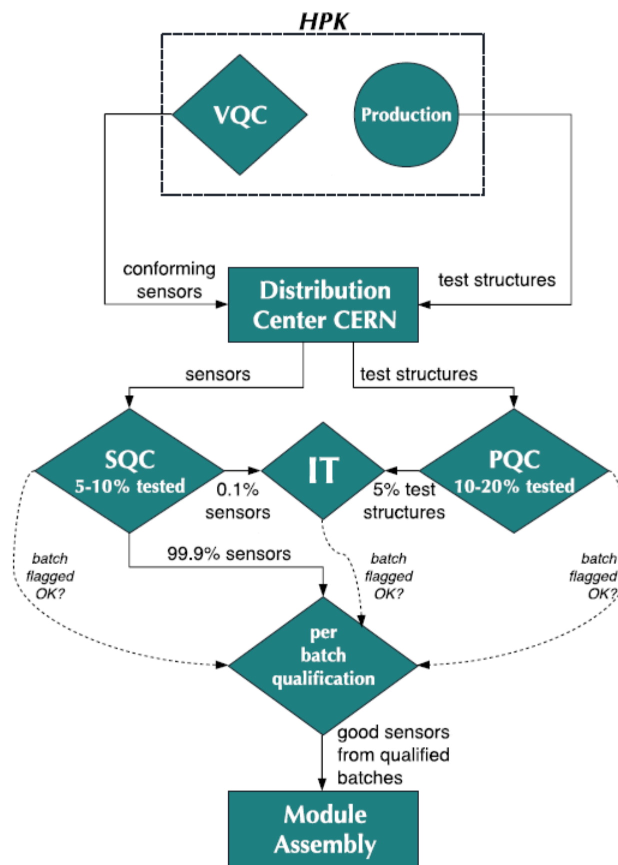

Figure 9: Process flow of the sensor QA for the CMS Phase-2 upgrade of the Tracker. For the HGCAL, a similar procedure will be applied.

tests to ensure that the radiation hardness is maintained. These sensors cannot be used for the final detector.

Die approbierte gedruckte Originalversion dieser Diplomarbeit ist an der TU Wien Bibliothek verfügbar
The approved original version of this thesis is available in print at TU Wien Bibliothek.
TU WIEN Bibliothek Your knowledge hub

4 Process Quality Control

As already addressed in the previous sections, over 50000 new silicon sensors will be manufactured and integrated in the CMS detector in the following years, which requires reliable testing methods to ensure their quality and the stability of production parameters. Process Quality Control (PQC) tracks the quality and reliability of the sensor production process by measuring process parameters on a dedicated set of test structures. Along with various other Institutes, HEPHY Vienna participates in PQC measurements of test structure sets for the CMS Tracker and HGCAL. The PQC test structure sets are located on the cut-off regions of the same wafers as the sensors and therefore show the same properties. Specific test structures exist for electrical measurements of a wide variety of parameters. Moreover, test structures allow to access parameters that cannot be measured directly on the sensors, including parameters that require destructive measurement methods.

4.1 Setup and Measurement Procedure at HEPHY Vienna

The fully custom-made probe station for PQC in the cleanroom of HEPHY Vienna allows to perform manual as well as automated measurements using a 20-needle probe card that connects to a contact pad set, referred to as flute. The flutes are organized in two rows of ten contact pads aligned in a 200 µm grid. The contact pads are connected to the wafer. Further, the contacts are connected to a switching matrix (*Keithley 7072-HV* matrix cards in a *Keithley 707B* six-slot mainframe), which allows quick and software configurable measurements for automated PQC. The required measurement instruments are also connected to the switching matrix. These consist of a *Keithley 2410* Source Measure Unit (SMU), a *Keithley 6517B* electrometer for high-precision current measurements and a *Keysight 4980A* precision LCR meter. Figure 10 shows the custom-made PQC probe station in the cleanroom of HEPHY Vienna. Also the measurement control software (COMET) for measurement automation was developed at HEPHY and allows to define a series of multiple measurements on different flutes via configuration files. The goal for an efficient operation was, that a measurement plan can be created, whereat the chuck can be loaded with up to 8 PQC flute sets. For straightforward analysis of the PQC measurement data and extraction of the few parameters of interest for each measurement, a Python based automated analysis routine has been established. For more details on the function of the analysis scripts, reference can be made to [10].

4.2 Overview: Test Structure Set

The same PQC test structure set, as illustrated in Figure 11, is implemented on Tracker and HGCAL wafers which allows to establish a standardised testing routine for the whole CMS Phase-2 upgrade. The PQC test structure sets, along with various other test structures, are placed on the cut-off regions of each wafer around the sensor. The resulting cut-off segments are generally referred to as half-moons. For one set of test structures there exist four main flutes, that get typically measured. Each flute accesses several

Die approbierte gedruckte Originalversion dieser Diplomarbeit ist an der TU Wien Bibliothek verfügbar
The approved original version of this thesis is available in print at TU Wien Bibliothek.
TU WIEN Bibliothek Your knowledge hub

Figure 10: Probe station for PQC at HEPHY Vienna. From left to right: Controlling PC, instrument rack and switching matrix, camera monitor showing the 20 needles of the probe card and shielding box with a vacuum chuck for test structures.

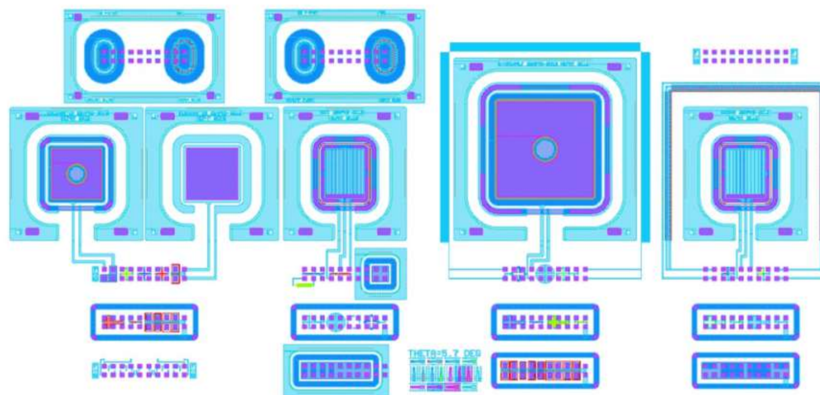

Figure 11: Layout of a full PQC test structure set.

large test structures (like Diodes, MOS Capacitors and so forth). Smaller structures (like Van-der-Pauw test structures) are contained within a flute. An overview of the typically measured PQC test structures and their respective, accessible process parameters is given in Table 2. Furthermore, the most important test structures and their measurement results get presented in more detail in the following.

Die approbierte gedruckte Originalversion dieser Diplomarbeit ist an der TU Wien Bibliothek verfügbar
The approved original version of this thesis is available in print at TU Wien Bibliothek.
TU WIEN Bibliothek Your knowledge hub

Test Struture	**Accessible Process Parameters**
Diode	Full depletion voltage, bulk resistivity, bulk doping concentration
MOS Capaitor	Flatband voltage, fixed oxide charge concentration, oxide thickness
Gate-Controlled Diode (GCD)	Surface generation current and velocity
MOSFET	Threshold voltage, p-stop doping concentration, implantation depth
Van-der-Pauw Structures	Sheet resistance of various materials and implants
Meander	Sheet resistance
Four-terminal resistivity test structure	Bulk resistivity
Cross-brigde Kelvin resistor (CBKR)	Contact resistance, specific contact resistivity
Contact chain	Process quality of contacts
Dielectric breakdown test structure	Breakdown voltage of the coupling dielectric

Table 2: Overview of the PQC test structures and their respective accessible process parameters.

4.3 PQC from Sensor Prototypes to Pre-Series

Contrary to the silicon sensors for the Tracker, which are already in production by the time of compiling the present thesis, the HGCAL is just about to start with sensor pre-production in 2023. For the HGCAL, the PQC measurement method has also proven to be useful during the sensor development phase to establish differences between different prototypes. The main focus within the scope of this thesis lays on the last prototypes (Version 2), which were produced, delivered and measured between February 2021 and May 2022, and the subsequent Pre-Series. For the Version 2 prototypes (ProtoA), the high-voltage stability was improved, compared to previous versions. Additionally, four different oxide variants (referred to as A, B, C and D) are tested for their suitability for the following Pre-Series. Since precise details of the process splits are not disclosed by Hamamatsu, the PQC measurements, in addition to other tests such as irradiation studies, are an important tool to find the most suited variant for the final production. Because the first ProtoA structures with oxide type A clearly showed insufficient properties, only the advanced oxide types B, C and D get compared in the following. Out of these three, oxide type C has been chosen for the Pre-Series and thus also for the final production. A further application of PQC described in this thesis consists in testing whether the agreed properties are consistently well maintained during the transition from prototypes to Pre-Series.

Die approbierte gedruckte Originalversion dieser Diplomarbeit ist an der TU Wien Bibliothek verfügbar
The approved original version of this thesis is available in print at TU Wien Bibliothek.
TU WIEN Bibliothek Your knowledge hub

4.4 Metal-Oxide-Semiconductor Capacitor (MOS-C)

The Metal-Oxide-Semiconductor Capacitor (MOS-C) is a well established test structure in semiconductor industry to access the properties of the Si-SiO_2 interface. It is composed of a planar metal gate electrode on top of the silicon bulk. In between, the SiO_2 layer serves as an insulator. For the PQC MOS-Capacitor, this layout gets complemented by a guard ring to shield the test structure from the influence of the surrounding structures. The PQC test structure set contains a square-shaped MOS-Capacitor with gate dimensions of 1.29×1.29 mm.

From a typical MOS-Capacitor's C-V characteristic measured at a frequency of 10 kHz (Figure 12b), the fixed oxide charge concentration, oxide thickness and flatband voltage can be extracted. For measuring the C-V characteristic, small negative to small positive gate voltages get applied while the device backplane is set to ground potential. Three specific regimes, referred to as accumulation, depletion and inversion, can be identified from the measurement curve. Accumulation occurs for negative voltages where holes are attracted to the semiconductor surface and the measured capacitance is determined only by the thickness of the oxide layer. The capacitance value C_{ox} is roughly constant at a maximum in this regime. The oxide thickness can be calculated using the formula for a parallel plate capacitor:

$$t_{ox} = \epsilon_0 \epsilon_r \frac{A_G}{C_{ox}}. \tag{6}$$

Here, $\epsilon_r = 3.9$ is the relative permittivity of the oxide and A_G is the gate area of the MOS-Capacitor. With increasing gate voltage, the energy bands flatten out until the intrinsic Fermi-level of the bulk is at the same potential as the Fermi-level of the surface. This configuration is referred to as *flatband condition*, with the respectively applied flatband voltage V_{fb}. In the PQC analysis of the MOS-Capacitor, the first derivative is formed and tangents are fitted around the maximum derivative and the low-slope region in the depletion region. Trough their intersection point, the flatband voltage V_{fb} can be extracted from the measurement. The fixed oxide charge concentration can be determined using

$$N_{ox} = \frac{C_{ox}(\phi_{MS} - V_{fb})}{qA_G}, \tag{7}$$

where $\phi_{MS} = \phi_M - \phi_S$ is the work function difference of the aluminium gate and the semiconductor. For the PQC analysis, $\phi_{MS} = -0.69$V is used. Exceeding the flatband voltage V_{fb}, the semiconductor is depleted of mobile carriers at the interface, which increases the effective thickness of the capacitor. Therefore, the capacitance decreases with the applied voltage. When further increasing the gate voltage, minority carriers (i.e. electrons) are attracted to the surface. In inversion, there exists a negatively charged inversion layer at the Si-SiO_2 interface in addition to the depleted region which shields the electric field from the gate. In this regime, the depletion layer remains at a constant thickness. A schematic cross section of a MOS-Capacitor with respective charge distribution in accumulation, depletion and inversion can be seen in Figure 12a.

Die approbierte gedruckte Originalversion dieser Diplomarbeit ist an der TU Wien Bibliothek verfügbar
The approved original version of this thesis is available in print at TU Wien Bibliothek.
TU WIEN Bibliothek Your knowledge hub

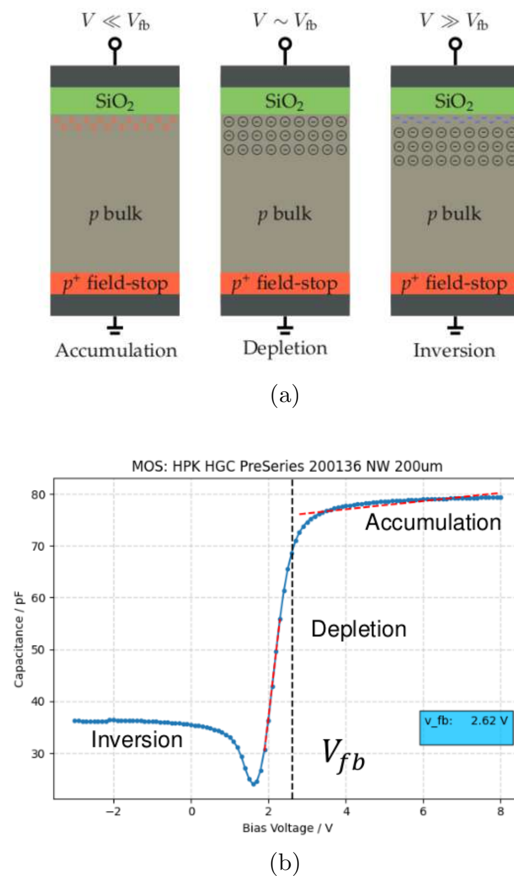

Figure 12: (a): Schematic representation of a MOS-Capacitor showing the charge distribution in the semiconductor during accumulation, depletion, and inversion. Courtesy of [19]. (b): Representative C-V measurement curve at 10 kHz with a fit to extract the flatband voltage V_{fb}.

4.4.1 Measurement Results

Figure 13 shows PQC MOS-Capacitor measurement results of the oxide thickness (13a) and the flatband voltage (13b). The plots include PQC data from approximately 100 HGCAL ProtoA wafers, where three different oxide types (B, C and D) get compared. Additionally included are measurements of the subsequent Pre-Series (approx. 55 wafers) with oxide type C, and Tracker results as a comparison. Since the Tracker sensors are already in production, it was possible to access results from the data base, not only measured by HEPHY but also other institutes, over the last two years. In total included is the data of approximately 1000 tested Tracker sensors. Because there is much more available Tracker data, the bars in the histograms are normalized and stacked for better visualisation.

Die approbierte gedruckte Originalversion dieser Diplomarbeit ist an der TU Wien Bibliothek verfügbar
The approved original version of this thesis is available in print at TU Wien Bibliothek.
TU WIEN Bibliothek Your knowledge hub

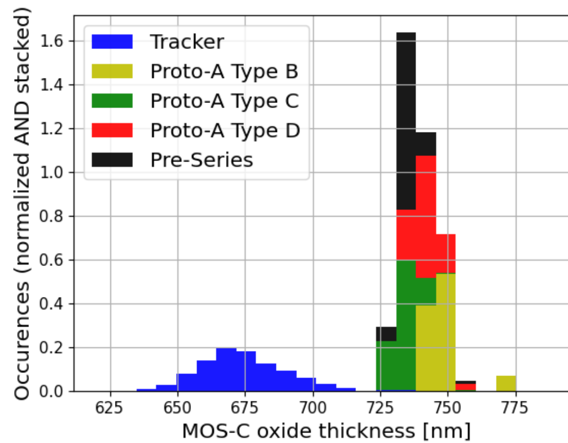

(a)

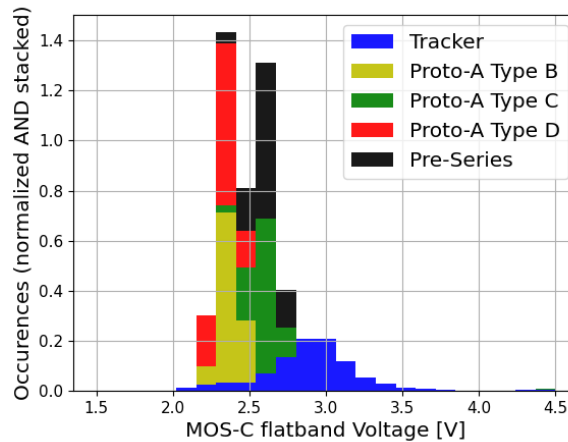

(b)

Figure 13: Histograms of MOS-Capacitor measurement results. (a): Oxide thickness, (b): Flatband voltage.

The MOS-Capacitor's oxide thickness ranges from values of 725 nm to 750 nm and shows no significant differences between the ProtoA oxide types and the Pre-Series. The Tracker shows on average smaller values but still in the same order of magnitude. This can come from slightly different production processes since for DC-coupled sensors, compared to the AC-coupled HGCAL sensors, the oxide thickness is of less relevance. Furthermore, the tracker results should only serve as a rough guideline. For the flatband voltage, there is good agreement between all ProtoA oxide types and the Pre-Series results with values around 2.5 V, which also nearly matches the Tracker data.

Die approbierte gedruckte Originalversion dieser Diplomarbeit ist an der TU Wien Bibliothek verfügbar
The approved original version of this thesis is available in print at TU Wien Bibliothek.
TU WIEN Bibliothek Your knowledge hub

4.5 Gate-Controlled Diode (GCD)

Gate-Controlled Diodes (GCD) are mainly used to separate the surface current component from the bulk current and allow to access process parameters like the surface generation/recombination velocity (which can be understood synonymously when assuming an uniform distribution of traps centered around the middle of the band gap [20]), interface trap density and bulk generation lifetime. They therefore provide information about the Si-SiO_2 interface quality. GCDs combine the properties of a diode and a MOS-Capacitor. The GCDs implemented on the PQC test structure set are built of a comb-shaped p-n junction bordered by an oxide-isolated metal gate. While the gate electrode is separated from the bulk by the oxide layer, the diode contact is routed directly through the SiO_2. A guard ring (n^+) and an edge ring (p^+) encircle the test structure. The PQC test structure set includes two GCDs with equal external dimensions and eleven gate strips. They differ in their gate widths of 50 µm for the Flute 2 *GCD* and 70 µm for the Flute 4 *GCD05*.

For a typical measurement of an I-V characteristic (Figure 14b), the diode is reverse biased at a fixed voltage V_{bias} (-5 V for PQC measurements) and the gate voltage V_{gate} is varied over a small range from the accumulation regime to inversion. In accumulation, holes are collected under the gate electrode and a depletion zone is formed under the n-doped region. In this regime, only the leakage current of the diode's space-charge region contributes, which means $I_{acc} = I_{bulk}$. With increasing the gate voltage, the diode current changes rapidly. The bulk area under the gate forms a depletion region, where the total leakage current is now composed of three current components

$$I_{dep} = I_{bulk} + I_g + I_{surf}. \tag{8}$$

Here, I_g denotes the leakage current generated by spontaneous pair creation under the gate and I_{surf} stands for the surface recombination contribution. The individual current components can contribute differently depending on the gate voltage. In the inversion regime, a thin inverted layer forms above the gate which prevents charge carrier creation at the surface. The surface recombination no longer contributes, so $I_{inv} = I_{bulk} + I_g$. This leads again to a change of the total diode current. The surface generation current can now be expressed in the following way:

$$I_{surf} = I_{dep} - I_{inv}. \tag{9}$$

The surface recombination velocity provides information about the concentration of recombination centres (i.e. traps) at the silicon-oxide surface. It can further be obtained from I_{surf} with

$$s_{surf} = \frac{I_{surf}}{A_G q n_i}, \tag{10}$$

where A_G is the gate area and n_i the intrinsic carrier density. When a uniform trap distribution as in [20] is assumed, s_{surf} relates linearly to the interface trap density. The bulk generation lifetime τ_g in the space-charge region beneath the GCD's gate can be related to the creation current I_g in a more elaborate way as discussed in more detail in [1].

Die approbierte gedruckte Originalversion dieser Diplomarbeit ist an der TU Wien Bibliothek verfügbar
The approved original version of this thesis is available in print at TU Wien Bibliothek.
TU Bibliothek WIEN Your knowledge hub

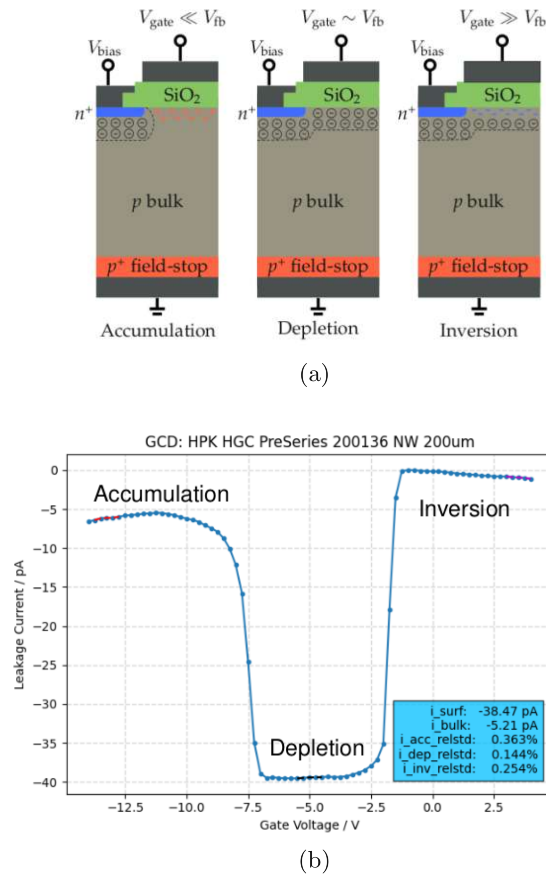

(a)

(b)

Figure 14: (a): Schematic representation of a GCD showing the charge distribution in the three regimes accumulation, depletion, and inversion. (b): Representative I-V measurement curve with $V_{bias} = -5\,\text{V}$.

4.5.1 Measurement Results

The parameter of interest for the GCD is the surface recombination velocity, since it allows to characterize the oxide quality through insight about the concentration of recombination centres. The results can be seen in Figure 15. Again, all three oxide types of the ProtoA test structures and the Pre-Series test structures with oxide type C show good agreement. For the Tracker, the majority of s_{surf} is generally lower. The higher values of s_{surf} for the HGCAL test structures could indicate a higher concentration of recombination centers. This parameter gets also investigated in irradiation tests, for which the GCD is sensitive, and still gives good results which are accepted for the final sensors.

Die approbierte gedruckte Originalversion dieser Diplomarbeit ist an der TU Wien Bibliothek verfügbar
The approved original version of this thesis is available in print at TU Wien Bibliothek.
TU WIEN Bibliothek Your knowledge hub

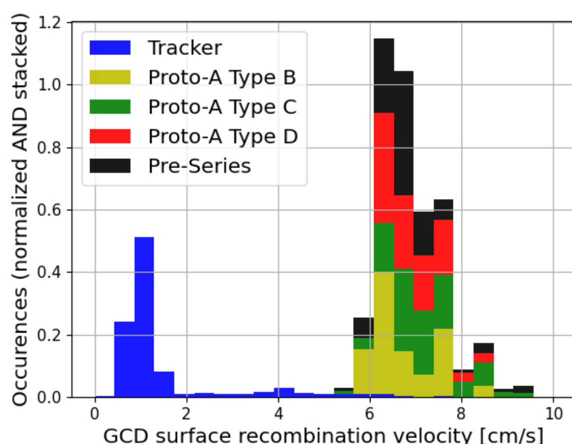

Figure 15: Histogram of GCD measurement results showing the surface recombination velocity.

4.6 Metal-Oxide-Semiconductor Field-Effect Transistor (MOSFET)

Metal-Oxide-Semiconductor Field-Effect Transistors (MOSFET) are well established devices in semiconductor electronics, whereas the application of MOSFETs in high energy physics as a test structure for silicon sensors is relatively new [21]. MOSFETs are based on a metal-insulator-semiconductor structure, i.e. a layered structure consisting of an insulated metallic gate electrode, a semiconductor and the oxide dielectric in between. The control of the PQC MOSFETs current flow in the semiconductor region is archived, as with all typical field-effect transistors, between the two electrodes drain and source. For the PQC MOSFET, the inter-channel region is spaced to replicate the inter-channel region of the final sensor including p-stop implants surrounding n^+ doped regions. The purpose of p-stop implants is to separate neighboring sensor channels. Therefor, the PQC MOSFET is an important tool to access inter-channel properties like the resistance between neighboring channels and the quality and implantation depth of the p-stop implant. The p-stop doping concentration can also be directly measured via the corresponding Van-der-Pauw test structure described in the following (Section 4.8). The PQC MOSFET is directly implemented within the flute of the test structure set, the schematic layout is shown in Figure 16a.

The parameter of interest, which is sensitive to variations of p-stop properties, is the MOSFETs threshold voltage V_{th}. It can be defined as the minimum gate-source voltage V_{GS} at which a current flow between source and drain gets established. For a typical PQC measurement, a small bias voltage of $-100\,\mathrm{mV}$ is applied between source and drain and V_{GS} is increased from small negative ($-2\,\mathrm{V}$) to small positive ($10\,\mathrm{V}$) values. The corresponding drain current gets measured. To extract V_{th} from a typical I-V measurement curve (Figure 16b), various methods are described in literature [22]. For

Die approbierte gedruckte Originalversion dieser Diplomarbeit ist an der TU Wien Bibliothek verfügbar
The approved original version of this thesis is available in print at TU Wien Bibliothek.
TU WIEN Bibliothek Your knowledge hub

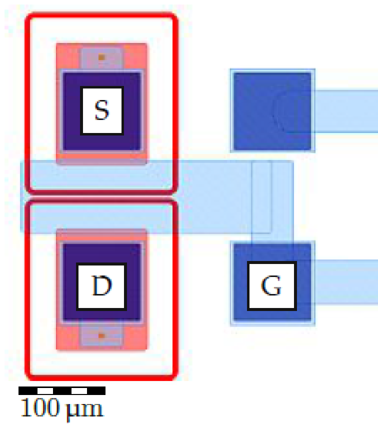

(a)

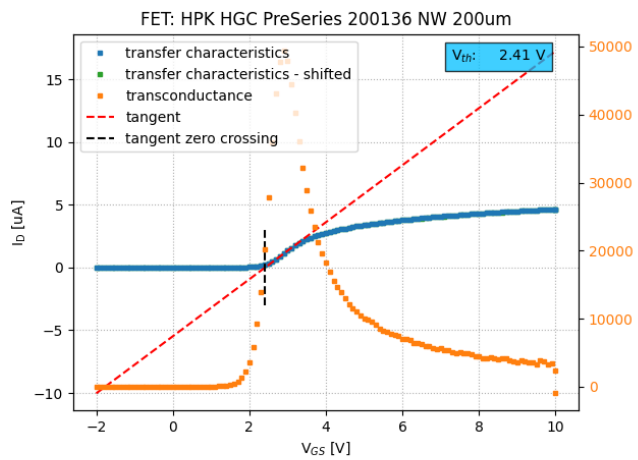

(b)

Figure 16: (a): Schematic MOSFET test structure contained within the PQC flute. The red framing around the electrodes source and drain represents the p-stop implant. (b): Representative measurement of the MOSFETs transfer characteristics with extraction of the threshold voltage V_{th}.

the PQC measurements, a method referred to as *extraction in the linear region* is used, which has the advantage of being comparatively robust. With this method V_{th} is given by the V_{GS}-axis intercept of the linear extrapolation of the I-V curve, at the point where the transconductance has a maximum. The transconductance is determined through the first derivative of the I-V measurement curve, as indicated in 16b .

Die approbierte gedruckte Originalversion dieser Diplomarbeit ist an der TU Wien Bibliothek verfügbar
The approved original version of this thesis is available in print at TU Wien Bibliothek.
TU Bibliothek Your knowledge hub WIEN

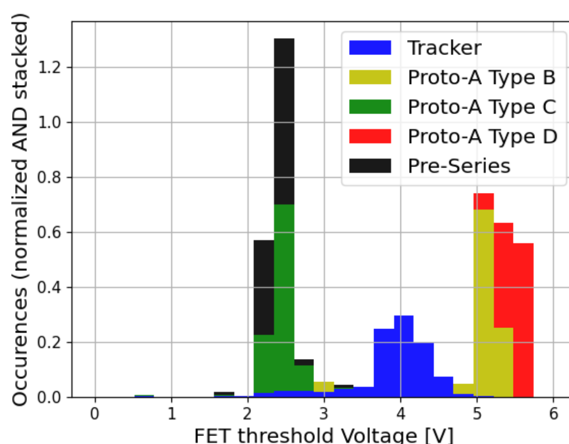

Figure 17: Histogram of MOSFET measurement results showing the threshold voltage.

4.6.1 Measurement Results

The histogram in Figure 17 shows the measurement results of the MOSFETs parameter of interest, the threshold voltage V_{th}. Again, HGCAL ProtoA and Pre-Series, as well as Tracker results, get compared to each other. V_{th}, which marks the voltage at which a conductive channel gets established between the electrodes and is therefore a measure for the inter-channel isolation, is higher for the tow tested oxide types B and D. ProtoA oxide type C and the Pre-Series, also produced with oxide type C, show similar behaviour. This can be understood as indication that the production process from ProtoA to Pre-Series is consistent. Nevertheless, lower values for V_{th} indicate that the inter-channel isolation is worse. Even though the unproblematic use of sensors with oxide type C is still out of question, the presentation of the present results was decisive for discussions among the community since the reason for the decrease of V_{th} for the newest oxide type C is not understood.

4.7 Device Simulation

Simulations of PQC MOSFET test structures were carried out using a TCAD based semiconductor simulation tool which allows to simulate any self designed 2D and 3D silicon device. IV and CV characteristics can be simulated with almost unlimited possibilities of varying the device properties by changing the doping concentration and profile, adding irradiation effects and many more. The design of the desired PQC test structure with corresponding doping and grid can be done first. Simulation tools then provide steady-state, transient, and small-signal analysis of arbitrary device geometries. Calculations are based on solving nonlinear equation systems at the intersection points of a self-defined grid over the device using the Newton procedure.

Die approbierte gedruckte Originalversion dieser Diplomarbeit ist an der TU Wien Bibliothek verfügbar
The approved original version of this thesis is available in print at TU Wien Bibliothek.
TU WIEN Bibliothek Your knowledge hub

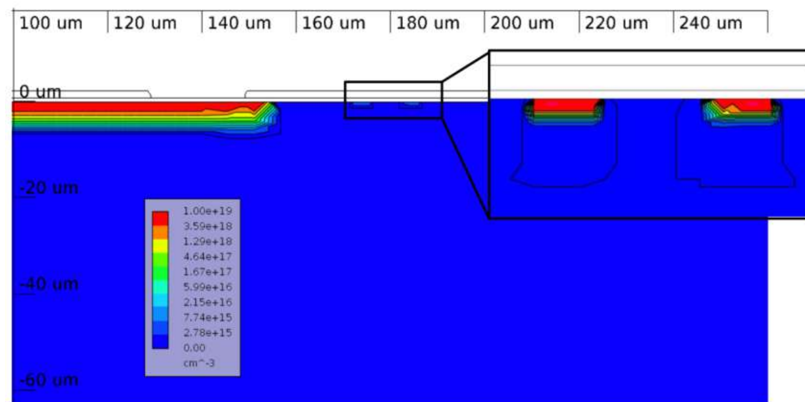

Figure 18: 2D model of a PQC MOSFET with doping used for device simulation. The p-stop implants are shown enlarged.

4.7.1 MOSFET Device Structure and Results

For simulations of the PQC MOSFET, a 2D model (Figure 18) gets used, with the advantage of less needed processing power and time compered to a 3D model. Since the objective of the simulations is to make qualitative statements about the behavior of the device, the accuracy of a 2D model is more than sufficient. The dimensions and spacing of the MOSFET electrodes and different implantations are taken from KLayout GDS files. Parameters like the oxide thickness can be extracted from PQC measurements. For the discussed simulation a mean measurement value of 750 nm is assumed for the oxide thickness. The doping of the n^+ and p-stop implants is implemented to the model with a Gauss-distributed. To obtain an I-V transfer characteristics, the voltage at the gate contact gets varied from small negative to small positive values, while the current at the drain contact gets measured. As in the PQC measurements, a small bias voltage of -100 mV between source and drain gets applied.

After creating the 2D MOSFET model, the influence of different parameters on the transfer characteristic can be investigated. Especially of interest are the properties of the p-stop implant. The first investigated parameter is the p-stop doping concentration. Starting with values obtained from PQC measurements, different increasing doping concentrations from $1 \cdot 10^{15}$ cm^{-3} to $1 \cdot 10^{16}$ cm^{-3} get simulated. As can be seen in Figure 19, with higher p-stop doping the resistivity of the implant decreases (correlation evident from equation 4) and therefore higher voltages are needed to obtain a conductive channel. The simulation shows a sensitivity of the PQC MOSFETs transfer characteristic to the p-stop doping concentration, as could be also observed in the PQC measurements. For another simulation, the spacing between the two p-stop implants in x-direction gets varied. The doping concentration of the p-stop implants is set to a constant value of $3 \cdot 10^{15}$ cm^{-3}. The distance d between the implants gets increased from the actual value of 6 µm to 26 µm and 46 µm. It can be seen in Figure 20 that the formation of a conductive

Die approbierte gedruckte Originalversion dieser Diplomarbeit ist an der TU Wien Bibliothek verfügbar
The approved original version of this thesis is available in print at TU Wien Bibliothek.
TU WIEN Bibliothek Your knowledge hub

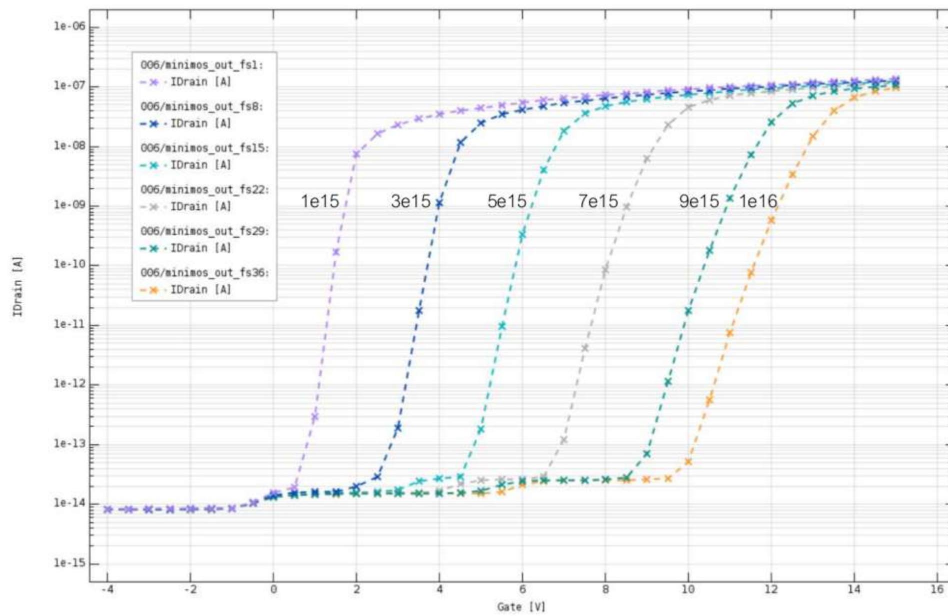

Figure 19: Simulated transfer characteristics of a PQC MOSFET with increasing p-stop doping concentration.

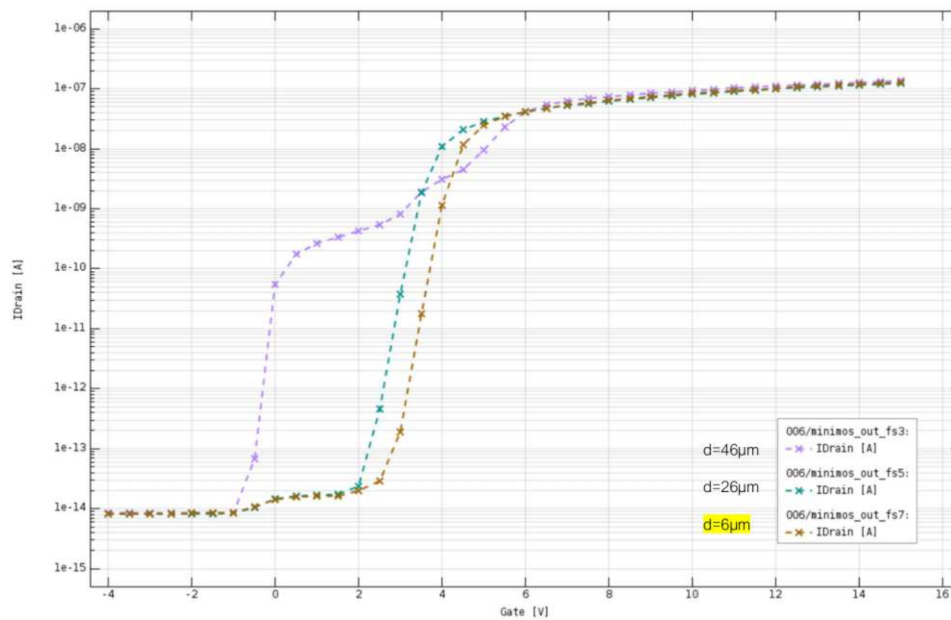

Figure 20: Simulated transfer characteristics of a PQC MOSFET with varying distance d of the p-stop implants.

Die approbierte gedruckte Originalversion dieser Diplomarbeit ist an der TU Wien Bibliothek verfügbar
The approved original version of this thesis is available in print at TU Wien Bibliothek.
TU WIEN Bibliothek Your knowledge hub

channel between the two electrodes shifts towards lower voltages with increasing distance of the p-stop implants. For the biggest simulated distance, the transfer characteristic even looses its typical shape.

4.8 Van-der-Pauw Structures

Van-der-Pauw test structures are commonly used to measure the electrical sheet resistivity of a thin and homogeneous (i.e. two-dimensional) sample of any arbitrary shape. The Van-der-Pauw method employs a four-point probe placed around the perimeter of the sample, which allows to provide an average resistivity of the sample independent of the geometry. CMS wafers include various Van-der-Pauw structures for different implantation types and materials, like the p-edge layer, p-stop and n+ implant, the polysilicon layer and the aluminum metalization. Shapes and dimensions vary with regards to available space on the wafer, whereas the most basic shape of the Van-der-Pauw test structure is a greek cross (Figure 21).

The sheet resistance is a useful parameter when considering thin samples. It can be related to the resistivity ρ and the thickness t of the considered thin sample with

$$R_{sh} = \frac{\rho}{t}, \tag{11}$$

where R_{sh} is expressed in the unit ohms per square. The resistance can then easily be calculated by multiplying R_{sh} with the length l per with w of the sample

$$R = R_{sh}\frac{l}{w}. \tag{12}$$

To determine the specific resistivity without knowing the current pattern in the sample, Van-der-Pauw proposed the following method

$$\rho = \frac{\pi}{\ln 2} t \frac{V_{34}}{I_{12}}, \tag{13}$$

where V_{34} is the voltage between contacts 3 and 4 and I_{12} is the current which flows from contact 1 to 2 [23]. Therefore, the sheet resistance can be expressed as

$$R_{sh} = \frac{\pi}{\ln 2}\frac{V_{34}}{I_{12}}. \tag{14}$$

In order to avoid errors that can come from imperfect contacts, it is possible to perform the resistance measurement a second time in a rotated configuration around the cross (V_{34}/I_{12}) and calculate the average between the two measurements.

4.8.1 Measurement Results

Figure 22 shows the p-stop sheet resistance measured from ProtoA, Pre-Series and Tracker PQC test structures. The threshold voltage V_{th} discussed above is connected

Die approbierte gedruckte Originalversion dieser Diplomarbeit ist an der TU Wien Bibliothek verfügbar
The approved original version of this thesis is available in print at TU Wien Bibliothek.
TU WIEN Bibliothek Your knowledge hub

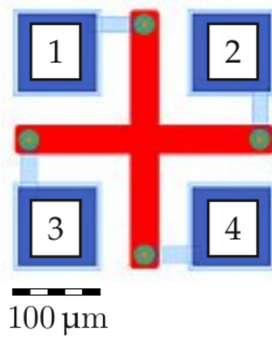

Figure 21: Schematic representation of the standard Van-der-Pauw cross directly contained within a PQC flute.

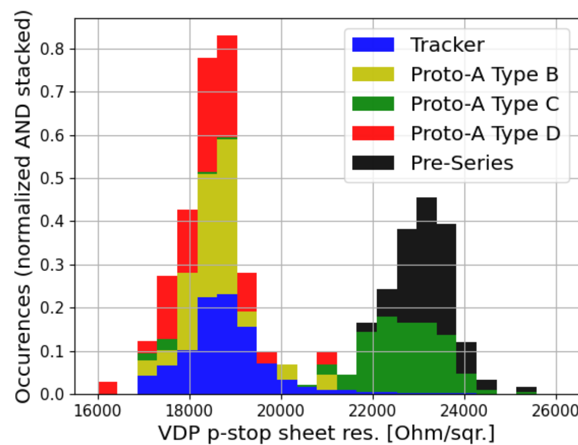

Figure 22: Histogram of Van-der-Pauw measurement results of the p-stop implant. The higher sheet resistance of the PtotoA oxide type C and Pre-Series samples can be correlated with lower MOSFET threshold voltages shown in Figure 17.

with the p-stop sheet resistance. The general correlation is that a higher p-stop doping concentration means lower p-stop resistance, better inter-channel isolation and therefore a higher threshold voltage. What can be seen from the results is therefore consistent with the previous findings. The ProtoA oxide type C and Pre-Series test structures have a higher p-stop sheet resistance that correlates to the lower threshold voltages seen before.

Histograms of further Van-der-Pauw results from the n-implant of the sensor (i.e. the strip sheet resistance) and the p-edge material are shown in Figure 23. For the n-implant (Figure 23a), ProtoA oxide type B behaves a little different and lays closer to the lower Tracker values than the other oxide types. Measurements of Proto-A type C and Pre-Series are consistent. For the p-edge sheet resistance (Figure 23b), there is good

Die approbierte gedruckte Originalversion dieser Diplomarbeit ist an der TU Wien Bibliothek verfügbar
The approved original version of this thesis is available in print at TU Wien Bibliothek.
TU WIEN Bibliothek Your knowledge hub

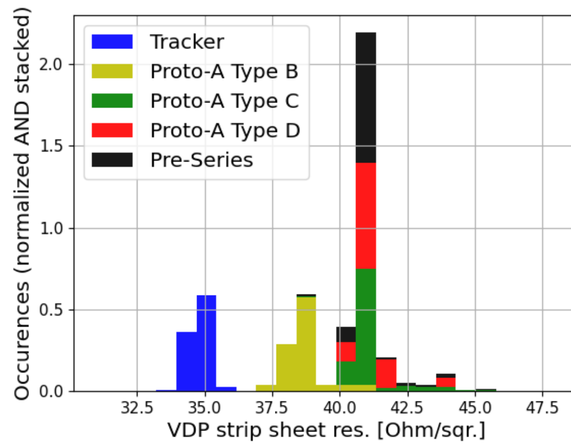

(a)

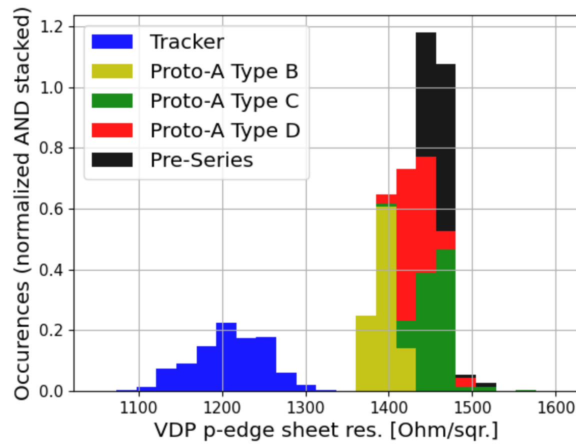

(b)

Figure 23: Histograms of Van-der-Pauw strip (a) and p-edge (b) sheet resistances.

agreement between all ProtoA oxide types and Pre-Series test structures. The Tracker sensors again have a little lower p-edge sheet resistances on average.

Die approbierte gedruckte Originalversion dieser Diplomarbeit ist an der TU Wien Bibliothek verfügbar
The approved original version of this thesis is available in print at TU Wien Bibliothek.
TU WIEN Bibliothek Your knowledge hub

5 Irradiation Tests

Irradiation studies of silicon sensors are an important way to identify their altered properties induced by hard radiation as experienced in the CMS detectors environment and impose stringent constraints in terms of their radiation resistance. The harsh radiation environment sets limits to the operability of silicon sensors, especially for the Phase-2 upgrade with its expected, high fluences. During the foreseen operation time, the irradiation induced changes in the silicon bulk will cause for example an increase of the necessary depletion voltage, dark currents and a decrease of the charge collection efficiency [14]. Surface damage can strongly influence inter-electrode isolation and breakdown of the detector [24]. A more detailed theoretical introduction to microscopic irradiation damage in silicon and the resulting macroscopic changes of sensor properties can be found in section 3.2. Neutron and X-ray irradiation campaigns of different PQC test structures have been carried out to investigate bulk and surface damage and the resulting changes of individual parameters.

5.1 Tests of Neutron Irradiated PQC MOSFETs

Neutron irradiation campaigns in the prototyping phase for the CMS Phase-2 upgrade are regularly conducted with HGCAL samples to investigate the altered bulk properties of the sensor material. During the compilation of this work, furthermore, the PQC test structure set was neutron irradiated for the first time. It could be shown, that the PQC measurement method is also applicable for irradiated samples, even though measurements have to be adapted and a new configuration file for the analysis is necessary, as already reported for a university project at HEPHY that preceded this thesis. In the following, especially the results of the irradiated MOSFET shall be discussed and later set in comparison with the results of X-ray irradiation studies of the same test structure.

5.1.1 Irradiation Facility, Measurement Setup and Samples

The neutron irradiation of test structures is carried out at a research reactor of the Jožef Stefan Institute (JSI) in Ljubljana. The institute runs a TRIGA Mark-II reactor developed by General Atomics. For the irradiation, the samples have to be put into plastic tubes and sent to the institute to be inserted into pipes, which guide the tubes down into the reactor core. For the tests, three ProtoA samples with a thickness of 120 µm were chosen (sensor IDs 300012, 300009 and 300032). The tested samples got exposed to the three following, increasing neutron fluences on the high end of the expected spectrum experienced in the CMS environment: $1.4 \cdot 10^{16}\,\mathrm{n_{eq}/cm^2}$, $1 \cdot 10^{16}\,\mathrm{n_{eq}/cm^2}$ and $5.5 \cdot 10^{15}\,\mathrm{n_{eq}/cm^2}$. To prevent annealing at room temperature, the irradiated structures were cooled before tested. Briefly before measuring, intentional annealing in the beneficial regime at 60 °C for 80 min in the climate chamber at HEPHY was performed. Since with irradiation the properties of the MOSFETs change and therefore also the targeted PQC process parameters, the measurement methods had to be adapted accordingly. The voltage ramp had to be increased for example, in order to measure the expected transfer characteristic.

Die approbierte gedruckte Originalversion dieser Diplomarbeit ist an der TU Wien Bibliothek verfügbar
The approved original version of this thesis is available in print at TU Wien Bibliothek.
TU WIEN Bibliothek Your knowledge hub

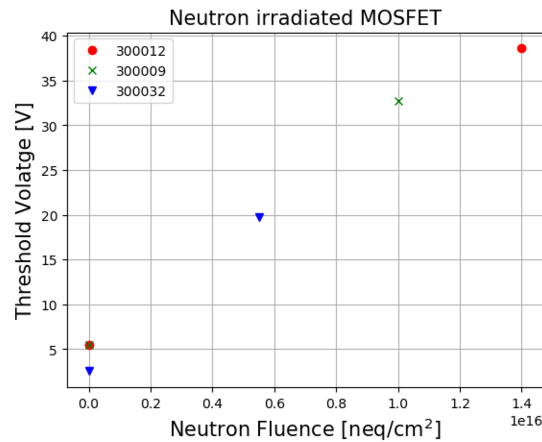

Figure 24: Change of the MOSFET threshold voltage for three ProtoA samples exposed to increasing neutron fluences.

5.1.2 Measurement Results

According to theory, with neutron irradiation, initially present donors get removed and the overall acceptor concentration increases as explained in section 3.2. The altered effective doping concentration of the silicon bulk results in changing bulk resistivity and therefore changing full depletion voltage towards worse performance of the device. As can be seen in Figure 24, the threshold voltage increases with higher exposed neutron fluence for the three tested ProtoA samples. This would mean, that the inter-channel isolation improves with irradiation. Some sources indicate that the oxide layer is also, to a non-negligible extent, influenced by neutron irradiation [25, 26]. Positive charges generated in the oxide could be a possible explanation for the observed, positive shift of the threshold voltage. Due to the small set of only three measured samples, which were all exposed to relatively high fluences, it is difficult to disentangle the individual effects which led to this results.

5.2 X-Ray Irradiation Campaign at CERN

Addressing the challenges of HL-LHC requires good understanding of surface damage due to the ionization energy loss of charged particles or X-ray photons. In particular, the complex phenomena related to the SiO_2 layer and the SiO_2-Si interface can be studied with X-ray tests of MOSFETs and GCDs from the PQC test structure set. Cumulative effects of oxide charge density and interface trap density change the parameters under consideration, such as the MOSFETs threshold voltage V_{th} and GCDs surface current I_{surf}. The high irradiation levels required to reproduce the expected, accumulated doses for the HL-LHC, combined with the need to maintain the duration of irradiation tests within a reasonable time span require a radiation source capable of providing high dose rates. To meet this requirements, the irradiation facility of the Electronics Systems for Experiments (ESE) group at CERN was used for the X-ray tests described in the

Die approbierte gedruckte Originalversion dieser Diplomarbeit ist an der TU Wien Bibliothek verfügbar
The approved original version of this thesis is available in print at TU Wien Bibliothek.
TU WIEN Bibliothek Your knowledge hub

following.

5.2.1 The ObeliX X-ray Facility and Measurement Setup

The ObeliX X-ray facility has been installed at CERN in 2017. It is equipped with a *Seifert RP149* X-ray generator with tungsten target, a beryllium window to seal the tube and aluminium filters to ensure uniform dose rates. The tubes maximum power supply voltage is 50 kV and the maximum tube current is 60 mA. Additionally, the custom-built setup offers a rectangular thermal plate, a *Huber Unistat 705* cooling element to set and maintain a dedicated temperature and a system to lower the dew point inside the irradiation cabinet using dry air from the compressed-air network. The thermal plate can be set to temperatures ranging from −50 °C to 200 °C, whereby the irradiation studies described in the following were carried out at 22 °C. The irradiation cabinet itself has a size of 102 × 102 × 76 cm. Moving the X-ray tube in vertical direction and the positioning of the DUT on the x-y plane can only be done manually. Lasers mounted on the X-ray tube allow to align the DUT with the beam center. No probe station is permanently installed in the cabinet, so the ObeliX X-ray facility can be used for diverse irradiation tests. An overview of the setup is give in Figure 25.

To observe the changed properties of the DUTs with irradiation, measurements were performed for increasing dose steps up to 100 Mrad directly in the irradiation chamber. The measurement setup (following the example of parts of the PQC setup used for MOSFET and GCD measurements) and software were built and tested at HEPHY before being transported to CERN. The instruments to perform in-situ measurements during the X-ray irradiation were placed on a table next to the ObeliX test chamber, with all cables coming from the provided cable pass-through. ObeliX can be controlled manually via a panel beneath the the test chamber. Alternatively, with a Python script the shutter of the X-ray tube can be closed remotely, a measurement performed and the shutter opened again in a few seconds. For controlling the X-ray tube and performing the measurements, a PC is used which is positioned next to the measurement instruments (Figure 26).

Two Source Measure Units (SMUs), a *Keithley 2410* and a *Keithley 2470*, were used as voltage sources for ramping and biasing, as well as for recording the drain current for the MOSFET tests. Both SMU models provide banana sockets for all outlets, so adapters have to be used to transfer the signal to common BNC cables that are connected to the DUTs via SMA adapters. An additional *Keithley 6514* electrometer for high-precision current measurements is included for the GCD tests, for which smaller currents in the pA-range are expected. The instrument allows reliable measurements of current levels down to 100 aA. Schematic representations of the circuits for MOSFET and GCD can be found attached in the Appendix. For monitoring the temperature, a PT100 mounted on every DUT gets read out by a *Keithley 2700* multimeter.

Die approbierte gedruckte Originalversion dieser Diplomarbeit ist an der TU Wien Bibliothek verfügbar
The approved original version of this thesis is available in print at TU Wien Bibliothek.
TU WIEN Bibliothek Your knowledge hub

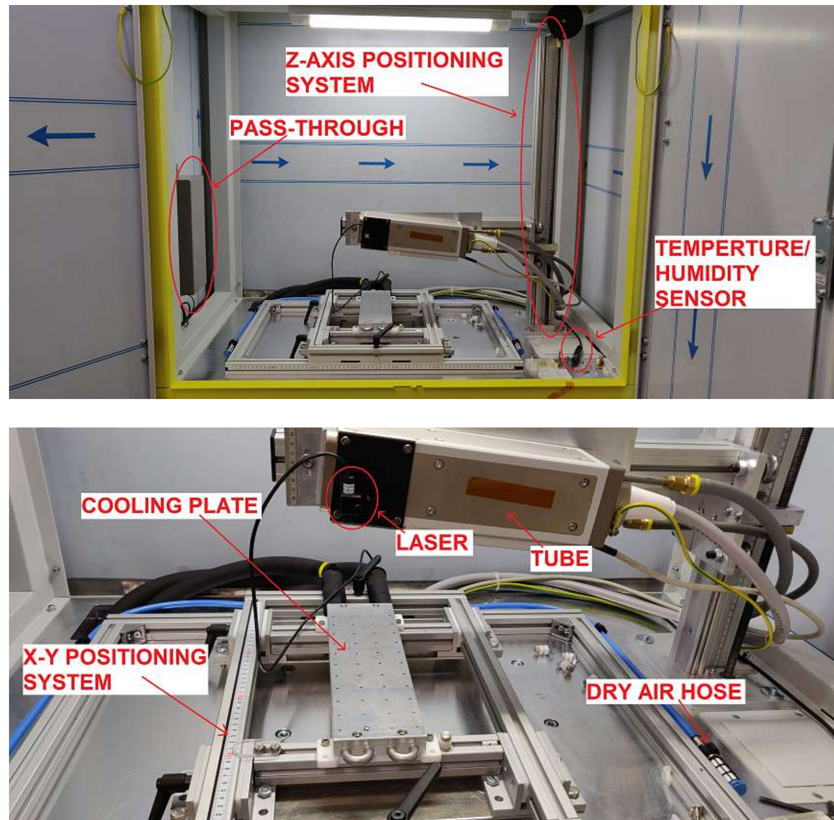

Figure 25: View inside the irradiation cabinet of ObeliX with pass-through for cables on the left side. The X-ray tube can be manually moved in the vertical direction. A laser fixed to the tube allows to precisely identify the position of the DUT with respect to the beam. Taken from [27].

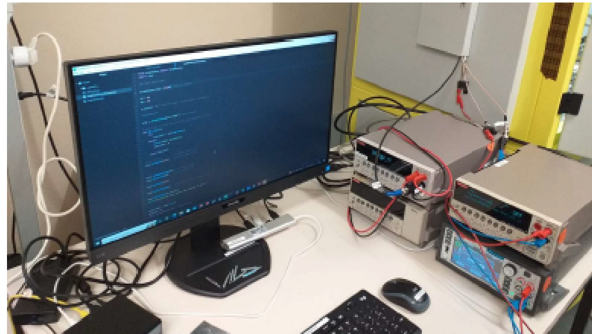

Figure 26: Measurement setup for X-ray studies next to the ObeliX irradiation chamber.

Die approbierte gedruckte Originalversion dieser Diplomarbeit ist an der TU Wien Bibliothek verfügbar
The approved original version of this thesis is available in print at TU Wien Bibliothek.
TU WIEN Bibliothek Your knowledge hub

Sample Name	Test Structure Type	Oxide Type	Thickness [µm]
200118 (Pre-Series)	FET	C	200
200136 (Pre-Series)	FET	C	200
4790_4 (Proto-A)	FET	B	300
4790_10 (Proto-A)	FET	B	200
4790_16 (Proto-A)	FET	D	300
VPX 35496_010 (Tracker)	FET	Tracker	290
200120 (Pre-Series)	GCD	C	200
VPX 35496_017 (Tracker)	GCD	Tracker	290

Table 3: List of samples for the X-ray irradiation study. Included are six MOSFETs and two GCDs from HGCAL and Tracker PQC test structure sets. The HGCAL samples include ProtoA and Pre-Series test structures with different oxide types, the Tracker samples serve mainly for comparison.

5.2.2 Samples

Measurements of in total eight different PQC test structures, as summarized in Table 3, were conducted during eight full days. From the whole test structure set, three MOSFETs with different oxide types from the HGCAL prototyping phase were tested. Additionally two MOSFETs and one GCD of the HGCAL Pre-Series were tested. As a comparison, two Tracker PQC test structures - one MOSFET and one GCD - were added to the irradiation campaign. The PQC test structure sets are fixed on ceramic PCBs, manufactured by the CERN SSD labs, with conductive silver glue. The contact pads of the dedicated test structures are wire bonded to soldered SMA connectors on the edges of the PCB. For the MOSFET, the source, drain and gate contact pads of the PQC flute are wire bonded to the connectors, for the GCD four bonds for the guard ring, gate, diode and backplane are needed. Each PCB has a PT100 sensor for temperature measurements mounted on top that is directly connected to a SMA adapter. 27. The PCB itself gets screwed on a copper base plate, which then is mounted on the ObeliX cooling plate in the irradiation chamber.
For the irradiation of the test structures the X-ray tube was set to 50 mA, 40 kV and positioned as close as possible (2.5 cm) above the sample to achieve a high dose rate and reduce the irradiation time. The final dose rate is 12 Mrad/h with a maximum variation of ±6.72%. The variation is extracted from a calibration map provided by the CERN ESE team. Since the spot size exceeds the size of the irradiation field to a considerable degree, the dose can be estimated as rather uniform over the whole irradiated test structure.

5.2.3 MOSFET Measurement Results

For the MOSFET measurements, the same bias voltage of 100 mV between drain and source as for PQC is applied. The voltage ramp has to be strongly increased up to 150 V for highly irradiated samples to clearly identify the transfer characteristic and extract the threshold voltage V_{th}. Figure 28 shows the MOSFET measurement scheme. Figure

Die approbierte gedruckte Originalversion dieser Diplomarbeit ist an der TU Wien Bibliothek verfügbar
The approved original version of this thesis is available in print at TU Wien Bibliothek.
TU WIEN Bibliothek Your knowledge hub

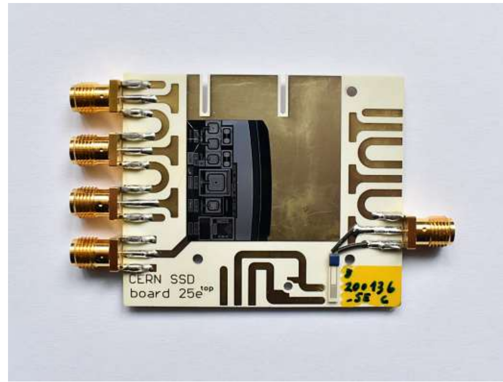

Figure 27: Ceramic PCB for X-ray irradiation test with PQC test structure mounted on top.

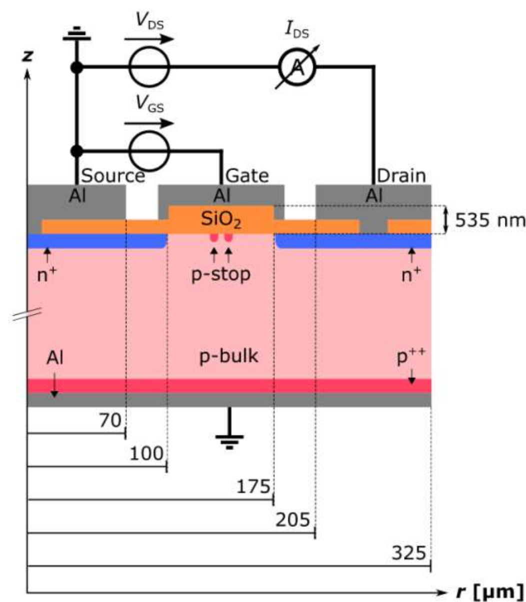

Figure 28: MOSFET measurement scheme adopted for the in-situ measurements of the transfer characteristic. Courtesy of [28].

29 shows the comparison of a measured MOSFET I-V curve before and after irradiation with 100 Mrad dose. It is evident that the I-V curve stretches out with higher levels of irradiation and that V_{th} is shifted to higher voltages.

Figure 30 shows the evolution of V_{th} of the five tested HGCAL MOSFETs with increasing X-ray dose. For the first irradiated sample, the bias voltage was just applied during a measurement but not in between tests during the X-ray irradiation. To prevent charge-up of the sample, for all following MOSFETs the bias voltage was applied during irradiation

Die approbierte gedruckte Originalversion dieser Diplomarbeit ist an der TU Wien Bibliothek verfügbar
The approved original version of this thesis is available in print at TU Wien Bibliothek.
TU WIEN Bibliothek Your knowledge hub

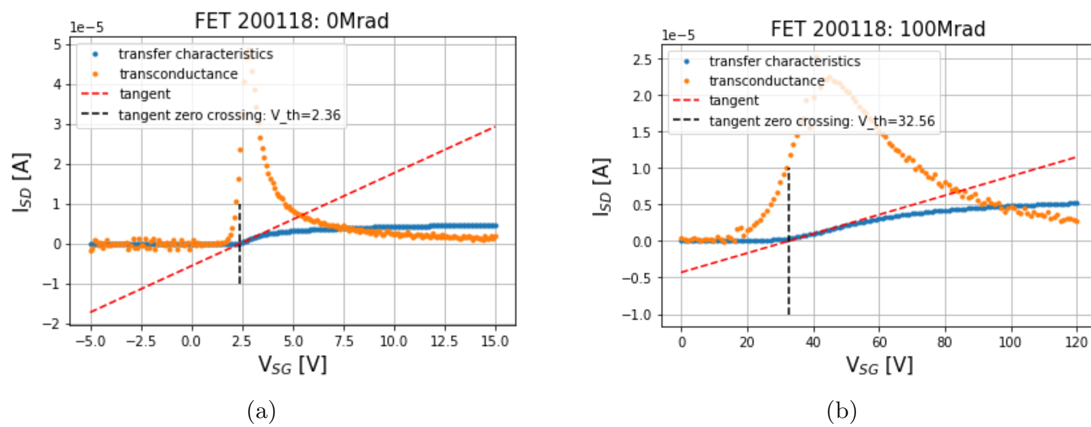

(a) (b)

Figure 29: MOSFET transfer characteristic at 0 Mrad (a) and 100 Mrad (b). The x-axis for the two plots differs, since the I-V curve is stretched out and shifted toward higher voltages after irradiation.

as well. Figure 30a shows all measured samples, which were biased during irradiation. The Pre-Series sample shows the lowest increase of V_{th}, the ProtoA sample with oxide type D shows the strongest increase of V_{th} up to 37.2 V. The two tested ProtoA samples with oxide type B show similar behaviour. Figure 30b compares the first measured Pre-Series sample, were the bias voltage was only applied during a measurement, with the second Pre-Series sample under constant bias voltage. It can be observed, that the increase of V_{th} with applied bias voltage only during measurement is pronounced stronger. The Tracker measurements of V_{th} with irradiation are not included in the plots, since a breakdown of the sample occurred only after 30 Mrad.

Because the measurements of V_{th} with increasing irradiation dose indicate that the values saturate at some point, irradiation up to 200 Mrad was carried out for some samples. Since the irradiation time was thereby increased up to 20 h, annealing effects cannot be neglected in the results. Therefore, these measuring points are omitted from the plots due to quantitative uncertainties. Qualitatively, it appears that complete saturation does not occur, but V_{th} continues to increase more and more slowly.

5.2.4 Interpretation

The shift of V_{th} towards higher voltages with increasing irradiation does indicate that the inter-channel isolation improves. Drawing comparisons with other studies of irradiated MOSFETs from literature proves to be difficult, as the framework conditions such as temperature, electric fields and oxide thickness vary significantly, but influence the measurement results up to a point that opposite effects can be observed [29]. The two competing effects are the positive oxide charge and the interface traps, which built up in the SiO_2 and the Si-SiO_2 interface due to electron-hole pairs. The former lead to a

Die approbierte gedruckte Originalversion dieser Diplomarbeit ist an der TU Wien Bibliothek verfügbar
The approved original version of this thesis is available in print at TU Wien Bibliothek.
TU WIEN Bibliothek Your knowledge hub

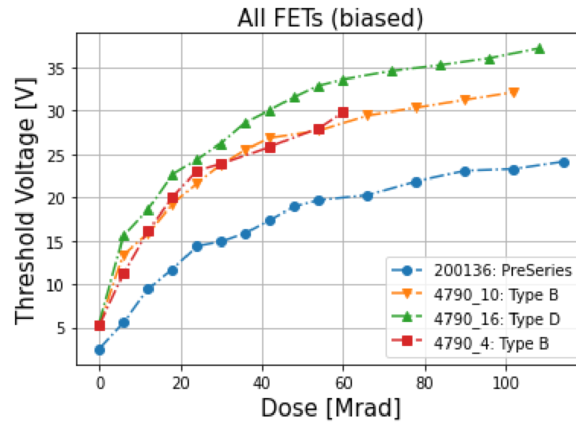

(a)

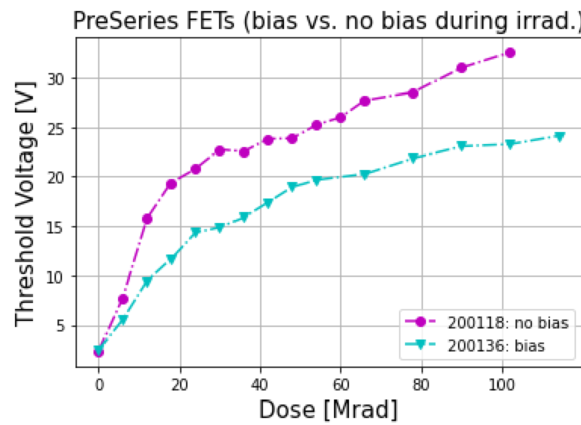

(b)

Figure 30: Change of the MOSFET threshold voltage with irradiation up to approx. 100 Mrad. (a): All HGCAL samples for which a bias voltage was applied during measurements and irradiation. (b): Comparison of Pre-Series samples with permanent bias and bias only during measurements.

negative shift of V_{th} and anneal fast at room temperature by tunneling of electrons from the silicon or thermal emission from the oxide valence band. The mainly acceptor-like interface traps in nMOSFETs on p-type substrate lead to a positive shift of V_{th}. For pMOSFETs this effect is reversed. Moreover, the effects of an increasing number of interface traps stretch out the I-V curve according to [30], which can be observed in the present study. For the interface traps no fast annealing is reported at room temperature [16]. In total, the shift of the threshold voltage is comprised of these two competing effects $\Delta V_{th} = \Delta V_{ox} + \Delta V_{it}$. In the study reported in [16], where conditions are to a large extent comparable with the here discussed measurements, similar results were obtained with the explanation that for a long low-dose-rate irradiation, a large fraction of the

Die approbierte gedruckte Originalversion dieser Diplomarbeit ist an der TU Wien Bibliothek verfügbar
The approved original version of this thesis is available in print at TU Wien Bibliothek.
TU WIEN Bibliothek Your knowledge hub

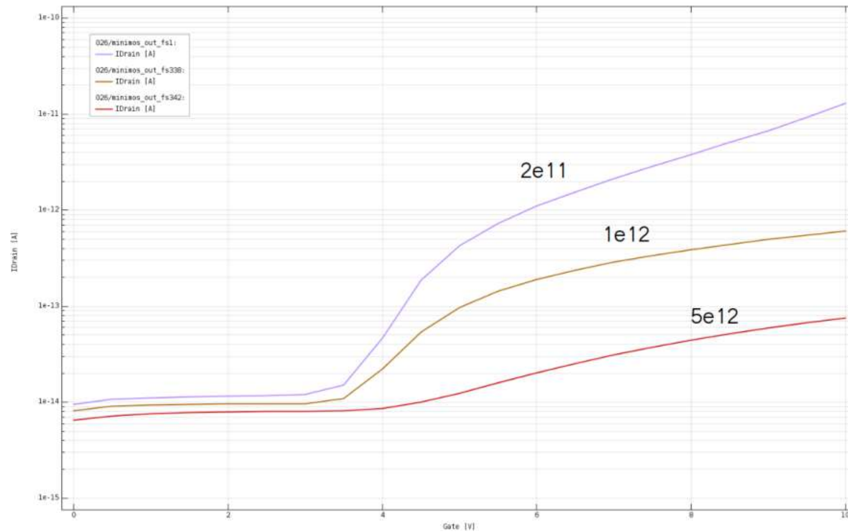

Figure 31: Simulated transfer characteristics of a PQC MOSFET with varying interface trap density.

oxide charges in the device may be neutralized already during irradiation. In contrast, the interface traps built up and saturate. This results in an overall positive increase of V_{th}, as can be also observed in the here described X-ray studies. Due to the large phase space of possible parameters to be varied, it is difficult to draw conclusions about the behaviour of the final sensors after irradiation from this small test group of PQC MOSFETs. More detailed measurements with targeted variation of certain parameters like the temperature could provide better understanding in the future building on these first observations.

5.2.5 Device Simulation

In order to better understand the effects of the X-rays induced oxide charges and interface traps on the test structures, a simple simulation can be carried out. Since the simulation of a realistic irradiation of the 2D MOSFET model would have required a long and intensive study of the TCAD-based simulation tool, a simplified approach was chosen. The semiconductor simulation tool offers the option to just increase the interface trap density. The same ramp and constant bias voltage as for previous simulations get applied. The interface trap density gets varied according to reported increases during X-ray irradiation from $2 \cdot 10^{11}$ cm^{-2} at 50 krad up to $5 \cdot 10^{12}$ cm^{-2} at over 100 Mrad in [24]. Figure 31 shows the simulation results. It can be observed, that the I-V curve gets stretched out, i.e. the slope of the curve with establishing of the conductive channel decreases, which would correlate to the behaviour of the tested MOSFETs for increasing doses. Determining the threshold voltage for the first two interface trap densities results in the same value of 3.5 V, whereby the absolute values may not exactly reflect the true measured values due to simplifying assumptions in the simulation. From the simulated

Die approbierte gedruckte Originalversion dieser Diplomarbeit ist an der TU Wien Bibliothek verfügbar
The approved original version of this thesis is available in print at TU Wien Bibliothek.
TU WIEN Bibliothek Your knowledge hub

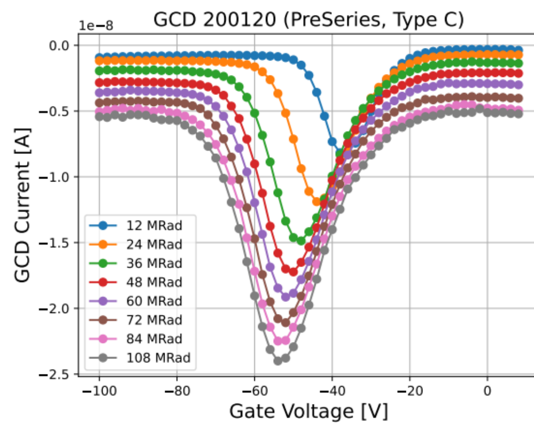

(a)

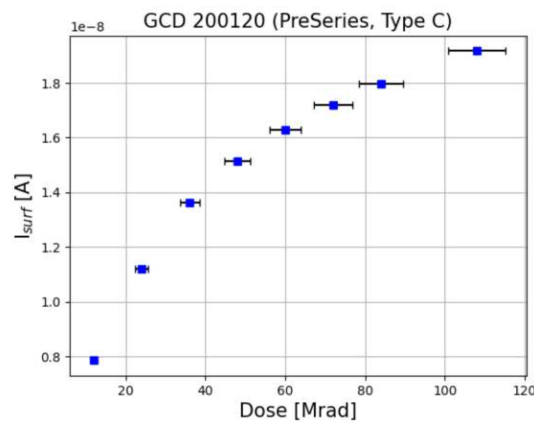

(b)

Figure 32: Measurements of the GCD surface current with increasing X-ray irradiation dose of an HGCAL Pre-Series sample. (a): I-V curves. (b): Extracted surface current values.

I-V curve for the highest density, it was not possible to determine a value for V_{th}, since no clear beginning of the increase is visible. The reason, that the shift of the threshold voltage towards higher values cannot be shown is probably due to the simplification of the simulation.

5.2.6 GCD Measurement Results

For GCD measurements with irradiation, the same bias voltage of 5 V as for PQC is applied. As for the MOSFET, the voltage ramp has to be increased to measure the characteristic I-V curve, from which the surface current I_{surf} can be extracted. Due to the strongly pronounced change of the I-V curve with irradiation, which was not known in advance, the measurement range was not chosen optimal for the first tested Tracker

Die approbierte gedruckte Originalversion dieser Diplomarbeit ist an der TU Wien Bibliothek verfügbar
The approved original version of this thesis is available in print at TU Wien Bibliothek.
TU Wien Bibliothek Your knowledge hub

GCD. Therefore, analysis was not possible for this sample. The I-V curves of the secondly irradiated Pre-Series GCD can be seen in Figure 32. It can be observed, that the I-V curves are strongly shifted towards negative voltages, already after the first irradiation step of 12 Mrad (Figure 32a). The minimum of a typical curve for non-irradiated GCDs lies usually around 5 V. I_{surf}, which is the current difference between depletion and accumulation regime, increases with irradiation (Figure 32b). The results for I_{surf} of the Pre-Series GCD can be compared to previous studies performed by the CERN HGCAL group. It is necessary to consider the temperature dependence of the I-V curve as described in [31], since the other HGCAL group performed their irradiation studies at lower temperatures. The Pre-Series sample exposed to X-ray irradiation and the previously tested ProtoA oxide type C sample, tested by the other HGCAL group, are in good agreement. In the present study, higher doses were achieved compared to previous GCD tests, which only showed the regime of steep increase of I_{surf}. From the here discussed results, it is evident that I_{surf} increases more slowly with higher doses.

5.3 Comparison of Neutron and X-ray Irradiation Results in Terms of Bulk and Surface Damage

Comparing the results of neutron and X-ray irradiation studies of the PQC MOSFET shows, that in both cases similar behaviour gets observed. The threshold voltage and therefore the formation of a conductive channel gets shifted towards higher voltage values. At first glance this result seems unexpected, as it would imply that in both cases the properties of the final sensor, in terms of inter-channel isolation, would improve with irradiation. Especially neutron irradiation, which mainly affects the bulk, is not expected to change a lot for the MOSFET, since its properties are mainly determined by the oxide layer. A positive shift of the threshold voltage is usually explained by changes in the oxide layer. Therefore, the results could imply that for such high neutron fluences the effects on the oxide layer are not negligible anymore. For the X-ray irradiated samples the positive shift of the threshold voltage can be induced by a the two competing effects of oxide charges and interface traps.

Die approbierte gedruckte Originalversion dieser Diplomarbeit ist an der TU Wien Bibliothek verfügbar
The approved original version of this thesis is available in print at TU Wien Bibliothek.
TU WIEN Bibliothek Your knowledge hub

6 Conclusion and Outlook

In the following years, the whole LHC is going to be upgraded to the HL-LHC to extend it's discovery potential. This upgrade will increase the LHCs luminosity, which makes it necessary to replace the detector systems so that they meet the requirements of the hard radiation environment. This also applies to the Tracker and new HGCAL of the CMS detector, were HEPHY is involved in the detector development for the upgrade. The Tracker and new HGCAL use silicon sensors for particle detection. Silicon as a semiconductor offers a lot of advantages for high energy physics like a low ionization energy, high position resolution and radiation hardness. The new silicon sensors must be tested during production to ensure that they meet the high requirements for the CMS Phase-2 upgrade and that the production process is stable over time. For this purpose, Process Quality Control as well as irradiation studies play a major role.

6.1 PQC Measurements

The first part of the present thesis is dedicated to PQC measurements of HGCAL ProtoA samples (with oxide types B, C and D) and the refined Pre-Series samples, delivered and measured at HEPHY from 2021 to 2022. With the PQC method, a set of test structures like MOS-Capacitors, MOSFETs and Gate Controlled Diodes can be tested to access specific process parameters. Particular attention is payed to the PQC MOSFET test structures, where TCAD-based simulations were carried out in addition to measurements. The PQC results presented in this thesis provided valuable input for the final prototyping phase of the HGCAL silicon sensors. Additionally, the reliability of the production process and the expected quality of the Pre-Series is confirmed. Comparisons show the convergence of the HGCAL properties towards the well established Tracker production process. PQC proved to be a very beneficial tool not only, as intended, during the series production of silicon sensors but also for characterization during prototyping. The silicon sensor pre-production for the HGCAL is scheduled to start in 2023.

6.2 Irradiation Studies

The second part of the thesis addresses the irradiation studies of the PQC test structure set. Such studies are particularly important for sensors of the CMS Phase-2 upgrade, which will need to sustain large particle fluences due to the increased luminosity of the HL-LHC. Neutron irradiation is usually carried out at a scientific reactor. The PQC samples were afterwards measured with a slightly adapted PQC procedure. The measurement campaign at CERN made it possible to test HGCAL PQC MOSFETs under the influence of X-ray irradiation for the first time. In order to carry out the X-ray studies, a measurement setup was assembled and tested within the framework of this work.

For both neutron and X-ray irradiation, similar behavior gets observed for the MOSFET: the shift of threshold voltage towards higher values and therefore the later formation of a conducive channel between electrodes. For the neutron irradiation, usually only bulk

Die approbierte gedruckte Originalversion dieser Diplomarbeit ist an der TU Wien Bibliothek verfügbar
The approved original version of this thesis is available in print at TU Wien Bibliothek.
TU WIEN Bibliothek Your knowledge hub

defects are expected. The comparison to the X-ray studies indicates, that the effects in the oxide for high neutron fluences also play a role.

For the X-ray irradiated MOSFET, the balance of the effects of oxide charges and interface traps could not be fully addressed within this thesis. Cumulative effects of oxide charge density and interface trap density can be disentangled thanks to specific data analysis procedures [30]. Further X-ray studies could be designed to measure the specific parameters required as input for such analysis procedures. Moreover, investigation of the influence of temperature, biasing and annealing on the PQC MOSFETs performance offer room for further studies.

Die approbierte gedruckte Originalversion dieser Diplomarbeit ist an der TU Wien Bibliothek verfügbar
The approved original version of this thesis is available in print at TU Wien Bibliothek.
TU WIEN Bibliothek Your knowledge hub

Appendix

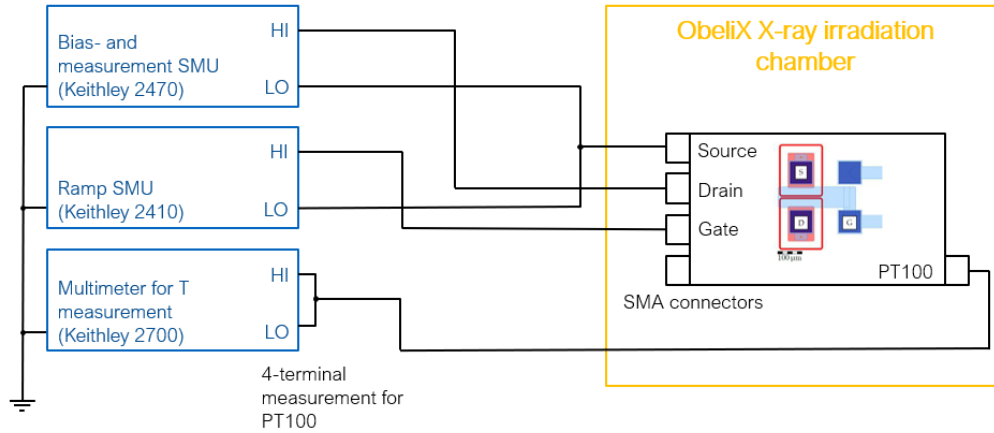

(a)

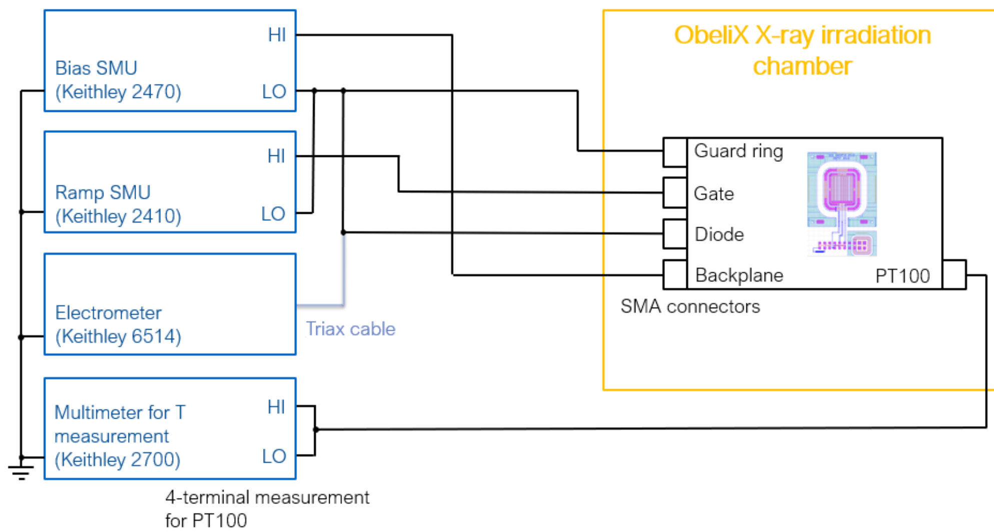

(b)

Figure 33: Schematic measurement setup for MOSFET (a) and GCD (b) X-ray irradiation studies with the ObeliX setup at CERN.

Die approbierte gedruckte Originalversion dieser Diplomarbeit ist an der TU Wien Bibliothek verfügbar
The approved original version of this thesis is available in print at TU Wien Bibliothek.
TU Bibliothek Your knowledge hub WIEN

References

1. Hinger, V. Silicon Sensor Process Quality Control for the CMS Phase-2 Upgrade. en. PhD thesis (TU Wien, 2021). https://repositum.tuwien.at/handle/20.500.12708/17013.
2. Sajot, G. *et al.* Experimental observation of isolated large transverse energy electrons with associated missing energy at $\sqrt{s} = 540\,\text{GeV}$. en. Publisher: CERN. http://cds.cern.ch/record/142059 (1983).
3. Arnison, G. *et al.* Experimental observation of lepton pairs of invariant mass around 95 GeV/c2 at the CERN SPS collider. en. *Physics Letters B* **126,** 398–410. ISSN: 03702693. https://linkinghub.elsevier.com/retrieve/pii/0370269383901880 (1983).
4. Collaboration, T. N. & Fanti, V. A new measurement of direct CP violation in two pion decays of the neutral kaon. en. *Physics Letters B* **465.** arXiv:hep-ex/9909022, 335–348. ISSN: 03702693. http://arxiv.org/abs/hep-ex/9909022 (1999).
5. Collaboration, T. C. Observation of a new boson at a mass of 125 GeV with the CMS experiment at the LHC. en. *Physics Letters B* **716.** arXiv:1207.7235 [hep-ex], 30–61. ISSN: 03702693. http://arxiv.org/abs/1207.7235 (2012).
6. Aad, G. *et al.* Observation of a new particle in the search for the Standard Model Higgs boson with the ATLAS detector at the LHC. en. *Physics Letters B* **716,** 1–29. ISSN: 03702693. https://linkinghub.elsevier.com/retrieve/pii/S037026931200857X (2012).
7. CMS Webpage. Accessed: 2022-11-20. https://cms-info.web.cern.ch/.
8. High Luminosity LHC Project Page. Accessed: 2023-01-03. https://hilumilhc.web.cern.ch/sites/default/files/HL-LHC_Janvier2022.pdf.
9. CMS, C. The Phase-2 Upgrade of the CMS Tracker. en. Publisher: CERN Document Server. http://cds.cern.ch/record/2272264 (2017).
10. Babeluk, M. Optimization and Qualification of the Process Quality Control for the Silicon Sensor Production of the CMS Phase-2 Upgrade. en, 81 pages. https://repositum.tuwien.at/handle/20.500.12708/18242 (2021).
11. Pree, E. Development of large area silicon sensors for the high granularity calorimeter at CMS. en. PhD thesis (TU Wien, 2018). https://repositum.tuwien.at/handle/20.500.12708/6976.
12. Thomson, M. Modern Particle Physics (University of Cambridge, 2013).
13. Huhtinen, M. Simulation of non-ionising energy loss and defect formation in silicon. en. *Nuclear Instruments and Methods in Physics Research Section A: Accelerators, Spectrometers, Detectors and Associated Equipment* **491,** 194–215. ISSN: 01689002. https://linkinghub.elsevier.com/retrieve/pii/S0168900202012275 (2002).
14. Moll, M. Radiation damage in silicon particle detectors: Microscopic defects and macroscopic properties. PhD thesis (Hamburg U., 1999).

Die approbierte gedruckte Originalversion dieser Diplomarbeit ist an der TU Wien Bibliothek verfügbar
The approved original version of this thesis is available in print at TU Wien Bibliothek.
TU WIEN Bibliothek Your knowledge hub

15. Junkes, A. Influence of radiation induced defect clusters on silicon particle detectors. PhD thesis (Hamburg U., 2011).

16. Schwank, J. R. *et al.* Radiation Effects in MOS Oxides. en. *IEEE Transactions on Nuclear Science* **55,** 1833–1853. ISSN: 0018-9499. http://ieeexplore.ieee.org/document/4636929/ (2008).

17. Adam, W. *et al.* P-Type Silicon Strip Sensors for the new CMS Tracker at HL-LHC. *Journal of Instrumentation* **12,** P06018–P06018. ISSN: 1748-0221. https://iopscience.iop.org/article/10.1088/1748-0221/12/06/P06018 (2017).

18. CMS, C. The Phase-2 Upgrade of the CMS Endcap Calorimeter. en. Publisher: CERN Document Server. http://cds.cern.ch/record/2293646 (2017).

19. König, A. Planar silicon strip sensors for the CMS phase-2 upgrade. en. PhD thesis (TU Wien, 2017). https://permalink.catalogplus.tuwien.at/AC14526557..

20. Grove, A. & Fitzgerald, D. Surface effects on p-n junctions: Characteristics of surface space-charge regions under non-equilibrium conditions. en. *Solid-State Electronics* **9,** 783–806. ISSN: 00381101. https://linkinghub.elsevier.com/retrieve/pii/0038110166901183 (1966).

21. König, A., Bergauer, T., Dragicevic, M. & Humann, B. Field effect transistor test structures for p-stop strip isolation studies. *Journal of Instrumentation* **12,** C02067–C02067. ISSN: 1748-0221. https://iopscience.iop.org/article/10.1088/1748-0221/12/02/C02067 (2017).

22. Ortiz-Conde, A. *et al.* A review of recent MOSFET threshold voltage extraction methods. en. *Microelectronics Reliability* **42,** 583–596. ISSN: 00262714. https://linkinghub.elsevier.com/retrieve/pii/S0026271402000276 (2002).

23. Van der PAUW, L. J. en. in *Semiconductor Devices: Pioneering Papers* 174–182 (WORLD SCIENTIFIC, 1991). ISBN: 978-981-02-0209-5 978-981-4503-46-4. http://www.worldscientific.com/doi/abs/10.1142/9789814503464_0017.

24. Moscatelli, F. *et al.* Surface damage characterization of FBK devices for High Luminosity LHC (HL-LHC) operations. en. *Journal of Instrumentation* **12,** P12010–P12010. ISSN: 1748-0221. https://iopscience.iop.org/article/10.1088/1748-0221/12/12/P12010 (2017).

25. Abdul Amir, H. F. & Chik, A. Neutron radiation effects on metal oxide semiconductor (MOS) devices. en. *Nuclear Instruments and Methods in Physics Research Section B: Beam Interactions with Materials and Atoms* **267,** 3032–3036. ISSN: 0168583X. https://linkinghub.elsevier.com/retrieve/pii/S0168583X09007137 (2009).

26. Amir, H. F. A., Chee, F. P. & Salleh, S. Effects of high energy neutrons and resulting secondary charged particles on the operation of MOSFETs. in *2014 International Conference on Computational Science and Technology (ICCST)* (IEEE, Kota Kinabalu, Malaysia, 2014), 1–6. ISBN: 978-1-4799-3241-2. http://ieeexplore.ieee.org/document/7045179/.

Die approbierte gedruckte Originalversion dieser Diplomarbeit ist an der TU Wien Bibliothek verfügbar
The approved original version of this thesis is available in print at TU Wien Bibliothek.
TU WIEN Bibliothek Your knowledge hub

27. ObeliX Webpage. Accessed: 2022-12-05. https://espace.cern.ch/project-xrayese/ObeliX/Forms/AllItems.aspx.

28. Hinger, V. *et al.* Field effect transistor test structures for inter-strip isolation studies in silicon strip detectors. en. *Nuclear Instruments and Methods in Physics Research Section A: Accelerators, Spectrometers, Detectors and Associated Equipment* **958,** 162233. ISSN: 01689002. https://linkinghub.elsevier.com/retrieve/pii/S0168900219307387 (2020).

29. Borghello, G. Ionizing radiation effects in nanoscale CMOS technologies exposed to ultra-high doses. PhD thesis (University of Udine, 2018).

30. McWhorter, P. J. & Winokur, P. S. Simple technique for separating the effects of interface traps and trapped-oxide charge in metal-oxide-semiconductor transistors. en. *Applied Physics Letters* **48,** 133–135. ISSN: 0003-6951, 1077-3118. http://aip.scitation.org/doi/10.1063/1.96974 (1986).

31. Zhang, J. *et al.* Investigation of X-ray induced radiation damage at the Si-SiO $_2$ interface of silicon sensors for the European XFEL. *Journal of Instrumentation* **7,** C12012–C12012. ISSN: 1748-0221. https://iopscience.iop.org/article/10.1088/1748-0221/7/12/C12012 (2023) (2012).

Die approbierte gedruckte Originalversion dieser Diplomarbeit ist an der TU Wien Bibliothek verfügbar
The approved original version of this thesis is available in print at TU Wien Bibliothek.
TU WIEN Bibliothek Your knowledge hub